

UNIVERSITY OF TWENTE.



princess máxima center

**3D Lab** |   
Radboudumc

# Evaluation of three dimensional visualisation techniques for improving preoperative planning of Wilms tumour surgery

*MSc thesis in Technical Medicine*

M. Fitski, BSc

University of Twente  
Department of Pediatric Surgery,  
Princess Máxima Center for pediatric oncology  
13 September, 2019



# Evaluation of three dimensional visualisation techniques for the preoperative planning of Wilms tumour surgery

M. Fitski, BSc

A thesis submitted to the University of Twente for the degree of  
Master of Science in Technical Medicine

**UNIVERSITY  
OF TWENTE.**



princess máxima center

**3D Lab** |   
Radboudumc

**Graduation committee:**

Prof. dr. ir. C.H. Slump (Chairman)  
Prof. dr. M.H.W.A. Wijnen (Medical supervisor)  
Dr. ir. F.F.J. Simonis (Technical supervisor)  
Dr. M. Groenier (Process supervisor)  
J.W. Meulstee, MSc (External member)



I dedicate this thesis to my family and girlfriend.

# Preface

Ruim zeven jaar geleden ben ik begonnen aan de opleiding Technische Geneeskunde. Na vier mooie jaren in mijn bachelorfase en een pittig eerste masterjaar, is mijn tijd in Enschede voorbij gevlogen. In Utrecht heb ik tijdens mijn eerste stage een passie voor chirurgie ontwikkeld. Tijdens mijn derde stage bij kinderradiotherapie besepte ik me dat de combinatie van kinderzorg en chirurgie weleens heel goed bij mij zou passen. In mei 2018 heb ik contact opgenomen met prof. Wijnen met de vraag of ik stage kon lopen bij zijn vakgroep, destijds nog in het Wilhelmina Kinderziekenhuis. Na een introductiegesprek kon ik beginnen met de stage. Ik heb gekeken naar wat er moest gebeuren om verdere stappen te nemen in de ontwikkeling van 3D anatomische modellen bij de preoperatieve planning. Na een succesvolle stage hebben wij, Marc Wijnen en ik, besloten dat we er meer werk van wilden maken en zijn we gestart met mijn afstudeerjaar, met de ideeën die zijn voortgekomen uit die stage. Ik heb veel kunnen bijdragen binnen de afdeling kinderoncologische chirurgie en ontwikkelingen binnen de onderzoeksgroep naast het schrijven van mijn scriptie.

Door mijn kennis over de kinderoncologische chirurgie te verbreden heb ik kunnen bijdragen aan veel verschillende casuïstiek. Zo heb ik pre- en intraoperatief kunnen bijdragen aan de oriëntatie van de chirurg met 3D anatomische modellen en deze op de juiste manier te visualiseren. Naast voor meerdere niertumoren heb ik dit gedaan voor kinderen met een kiemceltumor in het bekken, een weke-delen sarcoom in het onderbeen en bij een lever tumor. Door op niveau mee te kunnen praten en de juiste vragen te stellen heb ik modellen gemaakt waar de chirurgen en daarmee de patiënten echt iets aan hadden.

Daarnaast is het gelukt om een nieuwe sequentie toe te voegen aan de preoperatieve MRI van kinderen met Wilms tumoren. Door nauwe samenwerking met de afdeling radiologie en laboranten hebben wij de toegevoegde waarde van een non-contrast MRA sequentie kunnen laten zien. We zijn nu bezig met de laatste overleggen om dit klinisch toe te voegen aan het radiologisch protocol. Dit betekent dat kinderen met complexe niertumoren nu geen additionele CTA meer krijgen en daarmee een vermindering van anesthesie, straling, contrast en stress voor de patiënt. Daarmee hebben we concreet de patiëntenzorg kunnen

verbeteren.

Samen met het 3DLab van het RadboudUMC heb ik vorm gegeven aan de ontwikkeling van software voor augmented reality visualisatie van 3d anatomische modellen. Ik heb de software van het 3DLab klinisch gebruikt in samenwerking met de chirurgen, feedback verwerkt, ideeën bedacht en dit teruggekoppeld aan het 3DLab. Zo heb ik vorm gegeven aan onze samenwerking. Inmiddels is de software in een dermate vergevorderd stadium dat ik verwacht dat we preoperatieve plannings met behulp van augmented reality spoedig standaard in de kliniek kunnen gaan toepassen. Daarnaast heb ik ook de verantwoordelijkheid gekregen en genomen voor het gebruik van de 3D printer. Ik heb daar proactief nieuwe visualisatie technieken mee ontworpen. Deze 3D modellen zijn makkelijk mee te nemen naar de operatie kamer en helpen daardoor bij de intraoperatieve oriëntatie.

Als laatste heb ik mijn toegevoegde waarde kunnen laten zien op de afdeling door in nauwe samenwerking met de chirurgie te laten zien wat de toegevoegde waarde van een TGer is. Door technische ontwikkelingen toe te passen binnen het hele operatieve proces, van beeldvorming tot pathologische evaluatie, en niet alleen binnen het preoperative kader, heb ik mijzelf nuttig gemaakt bij ingewikkelde casuïstiek. Inmiddels word ik regelmatig bij patiënten betrokken en gevraagd om mee te denken en te helpen waar mogelijk.

Door verschillende projecten op te pakken heb ik mijzelf heel allround kunnen ontwikkelen en positioneren op de afdeling. Ik heb geleerd dat ik goed ben in klinische implementatie van beeldvormende technieken. Deze focus op het functioneler inzetten van bestaande technieken en alles daar om heen in goede banen leiden past goed bij mij als persoon en mijn interesses. Mijn rustige houding, observerend en analytisch vermogen en enthousiaste werkhouding hielpen mij hierbij.

Ik wil graag Marc Wijnen bedanken voor de mogelijkheid om in dit centrum stage te lopen en om mijzelf te ontwikkelen binnen de afdeling Kinderchirurgie. Daarnaast wil ik uiteraard ook Frank Simonis en Jene Meulstee bedanken voor hun technische begeleiding en vele overleggen. Verder wil ik Marleen Groenier en Gerike Bulthuis bedanken voor de processmatige feedback en gezellige gesprekken gedurende mijn afstuderen. Als laatste wil ik ook graag dr. Lee bedanken voor alle klinische uitleg, sparmomenten en voor het bijbrengen van de fijn kneepjes van de chirurgie. In de toekomst hoop ik de ontwikkelde technieken klinisch toe te gaan passen om zo chirurgen beter voorbereid de operaties in te laten gaan. Ik hoop mij op communicatief en wetenschappelijk niveau verder te ontwikkelen en verheug mij op de komende PhD-periode.

# Abstract

## Nederlands

Wilms Tumor (WT) is de tweede meest voorkomende abdominale tumor op kinderleeftijd. Niersparende chirurgie (NSS) kan worden uitgevoerd bij specifieke patiënten, om zo de late effecten van de behandeling te verminderen. Het is echter lastig om vooraf te bepalen wanneer NSS mogelijk is en veilig kan worden uitgevoerd. Hiervoor zijn geen duidelijke indicaties. Chirurgen blijven terughoudend om sparend te opereren omdat een positieve chirurgische resectierand additionele radiotherapie en eventueel extra chemotherapie noodzakelijk maakt.

Wij hebben nieuwe medische beeldvorming technieken geïmplementeerd en geëvalueerd om een beter inzicht te krijgen in de patiëntspecifieke anatomie van 7 WT patiënten. Wij hebben een hoge resolutie MRA-scan zonder contrast (b-SSFP) geoptimaliseerd voor gebruik bij kinderen. Deze scans werden gebruikt om retrospectief anatomische 3D-modellen te maken van de arteriën, venen, tumor, nieren en het urineverzamelstelsel (UVS) met een hoge visualisatiegraad. Beide technieken zijn kwantitatief en kwalitatief beoordeeld.

Bij de b-SSFP sequentie zagen wij een significant verhoogde beeldkwaliteit van de intraparenchymale arteriën ten opzichte van de MRA met contrast en de standaard T2-W sequentie. We zagen geen significant veranderde CNR in vergelijking met de MRA met contrast.

De anatomische 3D-modellen verkregen met het MATLAB segmentatie algoritme werden vergeleken met 3D-modellen gegenereerd met 3DSlicer. De 3D-modellen van de arteriën waren robuust en van hoge kwaliteit. De 3D-modellen van de venen en het UVS waren van lage kwaliteit en kunnen nog niet gebruikt worden in de klinische praktijk. De tumor- en niermodellen waren van hoge kwaliteit en lieten een grote overlap zien tussen de twee modellen. Kortom, de kwaliteit van de 3D-modellen van de arteriën, tumor en nieren is goed genoeg voor klinisch gebruik.

B-SSFP en een segmentatie algoritme zijn succesvol geoptimaliseerd, ontwikkeld, geïmplementeerd en geëvalueerd. Wij willen verder gaan met de ontwikkeling van deze technieken en onderzoek doen naar hoe deze technieken een aanvulling kunnen zijn op de preoperatieve beoordeling van WT-patiënten.

## English

Wilms Tumour (WT) is the second most common abdominal solid tumour in children. Nephron Sparing Surgery (NSS) can be performed in specific cases, which is expected to reduce later risks of the treatment. However, there are no clear rules and insights which dictate when to perform NSS. Therefore, surgeons remain hesitant to perform this technique, as a positive surgical margin necessitates radiotherapy and possibly additional chemotherapy.

We implemented and evaluated contemporary imaging techniques in order to gain more insight in the patient-specific anatomy during the preoperative planning of WT patients. A high resolution non-contrast MRA (b-SSFP) scan was optimized for paediatric patients and scanned on 7 WT patients. These MRA's were used to retrospectively create highly accurate 3D anatomical models of the arteries, veins, urine collection system (UCS), tumour and kidney through a developed semi-automatic segmentation algorithm. Both techniques were quantitatively and qualitatively assessed.

The b-SSFP sequence showed a significant increase in image quality for the visualisation of the intraparenchymal arteries in comparison to a contrast-enhanced MRA and standard high resolution T2-W sequence. We found no significant difference in CNR of the renal artery and intraparenchymal arteries between b-SSFP and CE-MRA during the quantitative assessment.

The MATLAB algorithm models were compared with anatomical models computed with 3DSlicer. The 3D arterial models proved robust and showed a high model quality. The 3D vein and UCS models were of low model quality and unfit for clinical use. The 3D tumour and kidney models showed a high average DICE coefficient and high model quality. The arterial, tumour and kidney models were fit for clinical use.

We successfully developed, optimized, implemented and evaluated a NC-MRA sequence and segmentation algorithm to improve the preoperative visualisation of Wilms Tumour patient specific anatomy. We hope to further develop and use these techniques to study how they complement our preoperative patient-specific understanding.



# Contents

<b>Preface</b>	<b>iii</b>
<b>Abstract</b>	<b>v</b>
<b>1 Introduction</b>	<b>1</b>
1.1 Clinical background . . . . .	1
1.2 Research aim . . . . .	8
1.3 Outline . . . . .	9
<b>2 Technical background and development</b>	<b>11</b>
2.1 Balanced Steady State Free Precession . . . . .	11
2.2 Development of a semi-automatic segmentation algorithm . . . . .	19
<b>3 NC-MRA implementation and evaluation</b>	<b>25</b>
3.1 Methods . . . . .	25
3.2 Results . . . . .	28
<b>4 Implementation and evaluation of the segmentation algorithm</b>	<b>33</b>
4.1 Methods . . . . .	33
4.2 Results . . . . .	36
<b>5 Discussion</b>	<b>41</b>
5.1 Balanced Steady State Free Precession . . . . .	42
5.2 Development of the segmentation algorithm . . . . .	44
5.3 Clinical implications . . . . .	45
<b>6 Recommendations</b>	<b>49</b>
6.1 Short-term . . . . .	49
6.2 Long-term . . . . .	50
<b>7 Conclusion</b>	<b>53</b>
<b>Appendices</b>	<b>54</b>
A SIOP staging for renal tumours . . . . .	55
B Literature review pediatric NCE-MRA . . . . .	56
C Rigid alignment . . . . .	62
<b>References</b>	<b>63</b>
<b>Glossary</b>	<b>71</b>

# List of Figures

1.1	Schematic coronal overview of the average extraparenchymal and intraparenchymal renal vasculature, reproduced from Klatter et al. (2015) [1]. . . . .	5
1.2	Axial non-enhanced balanced gradient echo showing both extra- and intraparenchymal arteries in infants, reproduced from Sertorio et al. (2018) [2]. The arrow indicates the renal artery. . . . .	5
1.3	Schematic overview of the outline of this thesis. . . . .	9
2.1	A = schematic explanation of the inflow enhancement. After the 180° inversion pulse, the longitudinal magnetization (Mz) for all tissues within the volume of the pulse (yellow) are negative. While waiting for fresh inflowing arterial blood (red), the Mz of the inverted volume starts restoring the equilibrium (green), the speed of which is dependent on the T1 characteristics of the tissue (Equation 1). At TI, the longitudinal magnetization in the kidney is null and the kidney will produce little or no signal. As the b-SSFP is a steady state, the magnetization will remain constant in the imaged Field of View (purple). Additionally, a fat saturation slab is added to saturate fat from the abdomen (pink). B = overview of the position of the FOV and inversion pulse. Adapted from McRobbie et al. 2017 [3]. . . . .	13
2.2	Four MIP b-SSFP scans with inflow enhancement at different settings of the Inversion Time (TI); A = 250 ms (min value), B = 400 ms, C = 450 ms, D = 620 ms (max value, 90 % of RR interval). C shows the preferred saturation of the kidney and delineation of the intraparenchymal arteries. In A, we can not fully appreciate the intraparenchymal segmental arteries due to insufficient inflowing fresh arterial blood. B and C show a good saturation of the kidney and adequate inflow of arterial blood. . . . .	16
2.3	Two MIP b-SSFP with arterial inflow results of the same volunteer at a different FA; A = FA 50°, B = FA 90°; B shows a more homogeneous and slightly increased signal intensity in the renal arteries. . . . .	16

- 2.4 b-SSFP with arterial inflow with different saturation slab positions; A = saturation slab caudal of the kidney, B = saturation slab at a distance twice the slab thickness from the lower pole, C = a double slab caudal to the kidney, D = coronal FOV; . . . . . 17
- 2.5 Overview of the saturation slab positions. The FOV (yellow) consists of 50 slices measuring 2 mm each. The reconstructed slice thickness is 1 mm, resulting in a sagittal thickness of 5 cm. The FOV is orientated parallel to the renal artery going towards to the pathological kidney (not depicted). The inversion slab (blue) is situated right below the lower pole of the kidney. A saturation slab runs along the abdominal wall for fat suppression. . . . . 17
- 2.6 b-SSFP with arterial inflow with different motion compensation techniques; A = cardiac trigger, B = respiratory trigger, C = respiratory gate, D = respiratory gate and tracking; C shows a more homogeneous signal intensity in the renal arteries. . . . . 18
- 2.7 MIP b-SSFP scans with inflow enhancement of the same volunteer scanned with the resulting parameter settings; A = transverse plane, B = coronal plane, C = sagittal plane. . . . . 19
- 2.8 Complete schematic overview of the developed Wilms Tumour segmentation algorithm. The algorithm comprises of seven elements per model: the MRI sequence, Volume of Interest (VOI), pre-processing, segmentation, post-processing, alignment of the model segmentation and the creation of the 3D model. The blue boxes are automated algorithms; orange boxes are manual procedures; the colours in the 3D modelling box represent the actual colour of the 3D model. Filled lines are regular steps, the dotted lines visualize additional alignment steps. Prior to the tumour segmentation, the kidney VOI is determined in the T1-W sequence and this is rigidly registered with the kidney VOI in the T2-W sequence. The transformation matrix derived from the rigid registration is used to align the tumour VOI with the T2-W sequence. . 24
- 3.1 Result of the alignment and translational registration of the CE-MRA (moving) with the b-SSFP sequence (fixed) of patient 1. The left image is the resulting transverse MIP from the NC-MRA (b-SSFP). The figure in the middle shows the transformed CE-MRA and the right figure visualizes the result after spatial alignment and translational registration. Areas in white have the same intensity after registration; areas in green and magenta have different intensities, which is expected outside of the vasculature. . . . . 27

3.2	The transverse MIP images resulting from the implementation of the b-SSFP with arterial inflow sequence of seven Wilms Tumour patients. All patients had unilateral disease, except for patient 3 whom had a bilateral tumor. The MIPs clearly visualize all four arterial segments. Patient 5 had previously had a nephrectomy. Therefore, the only remaining renal artery is shown. In patient 2 and 6, the inferior vena cava can be appreciated. . . . .	30
3.3	Two coronal MIP images of the same patient (2a); left is the b-SSFP sequence and right is the CE-MRA sequence. Visually, there is an increase in contrast of the b-SSFP sequence at the level of the renal and segmental arteries in comparison to the CE-MRA. . . . .	31
3.4	Results from the quantitative evaluation of the b-SSFP sequence (blue) and the CE-MRA sequence (orange). The contrast-to-noise ratio (CNR) was derived through an adjusted method described by Tan et al. (2012) [4]. The CNR was measured at the level of the renal artery and at the intraparenchymal renal arteries in aligned transverse MIP images. The connected dots represent the same patient. . . . .	31
3.5	Results of the qualitative assessment of three MR sequences used for vasculature imaging; b-SSFP (blue), CE-MRA (orange) and T2-W (red). The radiologist scored four vasculature segments based on a 4-point scale; the aorta (segment I), main renal artery (segment II), extra- and intraparenchymal arteries (segments III and IV). The mean score is giving with 1 standard deviation. . . . .	32
4.1	3D anatomical models computed through the developed MATLAB segmentation algorithm (A) and derived with 3DSlicer (B) of patient 1. The $\diamond$ illustrates the FOV of the NC-MRA, set parallel to the renal artery. The $\star$ shows the difference in VOI of the arterial model between the MATLAB arterial algorithm and 3DSlicer. The $\bullet$ visualizes the observer-variation between the two segmentation techniques. . . . .	37
4.2	Results of the quantitative virtual phantom study. The DICE coefficient was measured between a binary virtual phantom and the segmentation algorithm result. The DICE coefficient was computed for different settings of $\sigma$ and $\tau$ in the arterial segmentation algorithm. The parameters $\sigma$ and $\tau$ are used to control the Frangi-filter; $\sigma$ is the "radius" of the Gaussian tubular structure and $\tau$ controls the output uniformity. A $\sigma$ and $\tau$ of respectively 2 and 0.5 showed the highest DICE coefficient (0.897). . . . .	38

4.3	Results of the quantitative evaluation of the tumour and kidney segmentation. The DICE coefficient was computed for the tumour (blue) and kidney (orange) segmentations resulting from the MATLAB segmentation algorithm and 3DSlicer. The DICE coefficients are given for the included seven patients. Patient 5 did not undergo the right sequences and FOV to complete the segmentation through the developed MATLAB algorithm. . . . .	38
4.4	Results of the qualitative assessment of two segmentation techniques for the anatomical modelling of WT patients; computed through a developed MATLAB segmentation algorithm (blue) and 3DSlicer (orange). The models were scored on a 4-point scale. The mean score is giving with 1 standard deviation. . . . .	40

## List of Tables

3.1	Overview of the clinical and scan parameters of 6 different patients. ECG = three-leads electrocardiogram; PPU = Physiological Pulse Unit. Patients are in chronological order. . . . .	29
3.2	Results of the quantitative and qualitative evaluation of the optimized b-SSFP sequence. The mean CNR of the renal (RA) and intraparenchymal segmental arteries (SA) are shown in the quantitative segment. In the qualitative segment, the mean score and one standard deviation as assessed by the radiologist is given for the different vasculature segments; the aorta (segment I), main renal artery (segment II) and the extra- and intraparenchymal arteries (segments III and IV). . . . .	32
4.1	Results of the quantitative reproducibility measurement. The DICE coefficient is given between three segmentations derived from the arterial segmentation algorithm at three different moments. The GT is the result which is considered the ground truth, SR is the result it is compared with. . . . .	39
A.1	SIOP staging for renal tumours, derived from Metzger et al. (2005) [5]	55



# Introduction

## 1.1 Clinical background

Wilms tumour (WT) accounts for 90 % of all paediatric renal tumours with an incidence of 0.7 out of 100.000 children under 15 years old [6, 7]. Even though the majority of these lesions are unilateral (uWT) and solitary, approximately 12 % of the patients have multiple lesions and 7 % has a bilateral (bWT) tumour [8]. uWT patients have an overall survival (OS) after treatment of 90 %, whereas the OS for bilateral disease is 80 %. Unfortunately, 15 % of the patients relapse, commonly within the first two years after treatment [9]. The mean age of presentation of uWT is 3.3 years old, patients with bWT are generally younger and have a mean age of 2.6 years old. [10]

WT is associated with several overgrowth syndromes, such as Beckwith-Wiedeman syndrome, Simpson-Golabi-Behmel syndrome and Perlman syndrome [11]. Children with a mutation in the *WT1* gene are predisposed for syndromes such as WAGR syndrome, Denis-Drash syndrome. An underlying syndrome in a WT patient does not necessarily reduce the prognosis of the treatment of the tumour. However, due to the increased risk for WT, it may alter the treatment. Syndromic patients have an increased risk for early and multifocal malignancies [12]. Therefore, they are commonly treated with an approach similar to patients with bWT requiring more sparing surgery.

### 1.1.1 Current treatment protocol

The Renal Tumour Study Group of the International Society of Paediatric Oncology (SIOP-RTSG) recently published the UMBRELLA protocol for the diagnosis and treatment of paediatric renal tumours [13]. Following the UMBRELLA protocol, WT patients are staged postoperatively. The staging is described in Appendix A. Patients  $\geq$  6 months old with unilateral localized disease (stage I-III) receive

preoperative chemotherapy, actinomycin D and vincristine, in order to downstage the tumour. Children below this age receive direct radical nephrectomy (RN). RN is the complete removal of the kidney with the tumour and is further described in Subsection 1.1.2. The tumour is not histologically staged before treatment. Fine-needle biopsy is only performed in the case of unusual clinical presentation or findings on imaging. Unfortunately, 17 % of the WT patients have metastatic disease (stage IV), of which pulmonary metastases are the most common [14]. Stage IV patients preoperatively receive a combined vincristine, actinomycin D and doxorubicin regimen with reassessment imaging after 6 weeks.

The UMBRELLA protocol advocates RN with locoregional lymphnode sampling for all non-syndromic uWT patients after neoadjuvant chemotherapy. Locoregional lymphnode sampling is performed for accurate postoperative staging of the disease. The average stage II and III tumour size (40 % of the patient population) after preoperative chemotherapy is 163 ml [12]. If the tumour has a volume < 300 ml, nephron sparing surgery (NSS) may be performed for non-syndromic uWT. NSS is the surgical removal of the lesion, while leaving the renal parenchyma intact. If the tumour has a volume of > 300 ml, NSS is solely performed if the surgeon expects a substantial amount of functional kidney tissue and if there is no lymph node involvement. bWT is conventionally surgically removed through a combination of RN and NSS. Due to the increased risk of a contralateral tumour in patients with syndromic uWT, these patients may be treated with NSS as well.

It is believed that NSS reduces the risk of early stage chronic kidney disease and risk of end-stage renal disease (ESRD) in comparison to RN [15]. This is especially relevant considering ESRD is the second most common cause of death of adults who survived paediatric kidney cancer [13, 16, 17]. Additionally, uWT patients have a 2 to 3 % risk of developing a contralateral tumour which significantly increases the risk of reduced renal capacity, especially after RN of the previously affected kidney [18]. However, NSS for the treatment of non-syndromic uWT is controversial. The main concern with NSS for non-syndromic uWT is the risk of positive resection margins, therewith upstaging the tumour and increasing the local recurrence rate [19]. Upstaging of the tumour necessitates local radiotherapy and possibly additional chemotherapy. In a prospective study, Wilde et al. (2014) concluded that NSS for uWTs (N = 91) had the same Event Free Survival (EFS) and OS as RN (N = 2709) [20]. However, they emphasize that surgeons remain hesitant to perform this surgical treatment and therefore the possibility of NSS needs to be determined on a case-by-case basis. In 2012, Cost et al. performed a pathological study on pre-chemotherapy uWTs after RN of 78 patients to determine the percentage of patients who are amendable for NSS. They found that 24.4 % of the specimen met the predefined pathological criteria for NSS [21].

However, they also stress that certain theoretical criteria can not be assessed during the preoperative assessment. The difference between this study and the study of Wilde et al. (2014) (3 % NSS of the patient population) shows the caution of surgeons and difficulties in preoperative assessment. Richards et al. (2018) report the largest cohort of patients with uWT who received a partial nephrectomy (N = 235) from the National Cancer Data Base from the United States. They showed that there was no significant difference neither in OS nor in margin status between NSS and RN in children treated with the Children's Oncology Group (COG) protocol. Positive surgical margins were seen in 15.7 % therewith upstaging the tumour and necessitating accessory radiotherapy after NSS [22]. Kieren et al. (2013) reported a single institution experience in NSS for bWT, again following the COG treatment protocol. 23.8 % out of 21 children had a positive resection margin yet this did not decrease the OS. [23] In the SIOP-RTSG prospective study from Wilde et al, 12 uWT patients (13.2 %) had a positive margin. The reported figures for NSS are remarkably similar to RN, most likely due to the significant preoperative hesitation of surgeons to perform NSS. This causes the surgeons to perform NSS in relatively low stage tumours, resulting in an inclusion bias between the two approaches. It remains unclear when and how NSS is safely performed for WT patients. Surgeons need to assess the 2D preoperative imaging in order to make a decision on a 3D pathology, which adds to the hesitation. Research on improved visualisation techniques for the preoperative assessment of WT patients is required to reduce this hesitation.

### 1.1.2 Surgical procedure

Radical tumour nephrectomy is a complete resection of the kidney with the tumour. The tumour and kidney are mobilized from the surrounding tissue and the renal artery, vein and urether are occluded with titanium clips. This allows safe and complete removal of the tumour without an incision in close proximity, minimizing the chance of tumour spillage. Additionally, lymphnodes in the area cranial to the vena renalis are sampled to allow accurate postoperative staging of the tumour. [24]

During nephron sparing surgery, the tumour mass is removed through excision around the tumour encapsulation. Intraoperative ultrasound is used to gain insight into the tumour-kidney border and vessels in the kidney parenchyma. This allows the surgeon to decide the dissection plane. Any vessels in close proximity of the tumour are occluded or circumvented. Prior to the resection, the renal artery and vein can be temporarily clamped with Bulldog clamps to reduce blood flow inside the kidney, therewith reducing blood loss. The duration of the clamping should be

kept at a minimum to reduce ischemia of the renal parenchyma. When the tumour is resected, absorbable sutures are used to close small vessels within the incised renal parenchyma. Again, lymph nodes are sampled to accurately determine the stage of the tumour. If necessary, the remaining kidney is fixated to the abdominal wall to prevent torsion. [25, 26]

### 1.1.3 Preoperative imaging

After neoadjuvant chemotherapy, a magnetic resonance imaging (MRI) scan is made for the preoperative assessment of the tumour and to determine the surgical treatment. Additionally, a high resolution CT thorax is made to assess any pulmonary nodules. As stated previously, according to the SIOP UMBRELLA protocol, the patient is eligible for NSS if the tumour has a volume  $<300$  ml. If the tumour has a volume of  $>300$  ml, NSS is only performed when the paediatric surgeon expects a substantial amount of functional kidney tissue and if there is no expected lymph node involvement. This assessment is challenging and requires extensive anatomical knowledge of the position of the tumour, extra- and intraparenchymal vasculature, tumour vasculature extension and the relationship of the tumour with adjacent surrounding tissue [1]. Additionally, the postoperative residual renal parenchyma seems crucial for adequate renal function and therefore anatomical volumetric knowledge is considered useful for the preoperative assessment [27]. The current MRI protocol possibly does not provide sufficient knowledge on the renal vasculature and anatomic relationships. A lack of adequate vasculature imaging and three dimensional information limit the preoperative visualisation. Generally, if NSS is expected to be feasible, an additional Computed Tomography Angiography (CTA) scan is made to understand the intraparenchymal vasculature. It visualizes the renal vasculature in relationship to the renal tumour at a high spatial resolution ( $0.48 \times 0.48 \times 1$  mm<sup>3</sup>). However, the radiation dose and injection of a contrast agent are a concern in our patient population [28]. Radiation increases the risk of cancer and contrast agents can cause allergic reactions and nephropathy. Therefore, safe and unburdening imaging techniques such as high resolution MRA's and 3D anatomical modelling, may be explored.

#### Magnetic Resonance Angiography

The current abdomen 1.5 tesla (T) MRI protocol in the Princess Máxima Center for paediatric oncology is a combination of T2-weighted sequences, fat-suppressed T1-weighted sequences (pre- and post-gadolinium administration), a diffusion weighted sequence and a contrast-enhanced 4D MRA (CE-MRA) sequence. The currently used CE-MRA sequence visualizes the main renal artery clearly, yet the

segmental branches are difficult to appreciate. This is considered insufficient visualisation of the renal vasculature for the preoperative planning for NSS [29]. The segmental arteries and intraparenchymal arteries, as depicted in Figure 1.1, are not clearly visualized. Nevertheless, the segmental arteries are essential and the intraparenchymal arteries are meaningful for the preoperative planning for NSS.

The CE-MRA sequence is currently not able to visualize important renal vasculature due to multiple limitations. The CE-MRA is partially limited by the contrast agent, which quickly flows inside the parenchyma making it unfeasible to depict intricate intraparenchymal arteries. On top of that, the usage of gadolinium based contrast materials (GBCM) should be avoided in patients with a reduced renal function because of an increased risk of nephrogenic system fibrosis, despite the fact that GBCMs are generally considered safe for children [30–32]. Finally, it requires skilful timing of the MR operator and even so, the renal arteries are very difficult to visualize. The MR operator has to start of the sequence when the GBCM enters the descending aorta based on a 3D (2D image scanned over time) scout image. Due to the 4D characteristics of the CE-MRA sequence and the low contrast dose used in paediatrics, the image quality and resolution are relatively low.

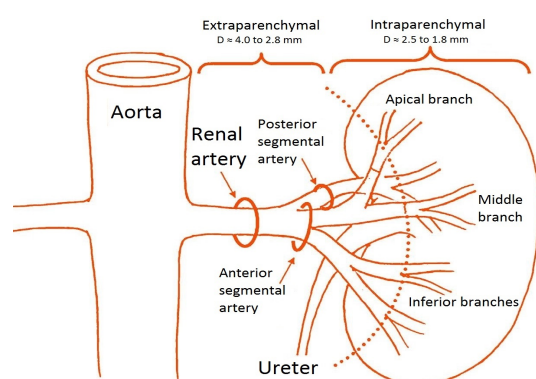


Figure 1.1: Schematic coronal overview of the average extraparenchymal and intraparenchymal renal vasculature, reproduced from Klatt et al. (2015) [1].



Figure 1.2: Axial non-enhanced balanced gradient echo showing both extra- and intraparenchymal arteries in infants, reproduced from Sertorio et al. (2018) [2]. The arrow indicates the renal artery.

A different renal MRA sequence may be required to address the problems with the CE-MRA for the visualisation of the intraparenchymal arteries. An user-independent and contrast free MRA sequence may be of added value for the visualisation of the extra- and intraparenchymal arteries. Non-contrast MRA (NC-MRA) is not yet commonly used to visualize the extra- and intraparenchymal arteries in paediatrics. However, for this objective, balanced Steady State Free Precession (b-SSFP) with arterial inflow has been previously described [2, 33–35].

The results of these studies using b-SSFP for imaging of renal vasculature in children were excellent and encouraging, yet showing limitations in young children due to the staircase artefact. An example of the usage of b-SSFP in children is given in Figure 1.2. A review of the literature can be found in Appendix B. The technical principles behind b-SSFP are further explained in the technical background in Chapter 2, Section 2.1.

Using inflow enhanced b-SSFP for paediatric renal oncological surgery has not been studied before, yet it is justifiable. Advantages of the sequence include a high signal-to-noise ratio (due to the combined signal from free induction decay and residual transverse magnetization), high contrast-to-noise ratio without adding a contrast agent and a fast acquisition time which allows high resolution visualisation. Additionally, the sequence is flow direction independent making it a useful technique for imaging of the multi-directional intraparenchymal arteries. One of the main disadvantages of b-SSFP is the limited field of view (FOV) which might be a concern in WT patients. Increasing the FOV is directly associated with a longer scanning time which is undesirable regarding the anesthesia in smaller children. More cranially or caudally situated arterial branches might not be fully encompassed by the FOV. This might affect our understanding of the vasculature, yet this is likely to be insignificant as these additional branches are also visualized through the standard high resolution T2-W.

### **Three dimensional anatomic modelling**

The NC-MRA can be used for the 3D anatomical modelling of renal tumours. 3D anatomical modelling is used increasingly for the preoperative planning for renal tumours due to improved and more accessible imaging, segmentation and visualisation techniques [36–42]. In adults, these models are used and have been proven to be useful for the preparation of minimally invasive surgery and NSS. An extensive systematic review illustrates the use of 3D printed models for adult renal surgery. They describe the positive surgical effects of 3D printed anatomical models such as reducing estimated blood loss, intraoperative complications and improving patient education. [43]

Studies on 3D anatomical modelling specifically for the preoperative planning of Wilms tumours are mostly on a case-by-case basis [44–47]. Fuchs et al. (2005) demonstrated they were able to create 3D anatomical model for four uWT patients [44]. They concluded that 3D anatomical models were of significant value in patients whom may need complex procedures. Girón-Vallejo et al. (2017) produced a model for NSS of a bWT to improve their understanding of the tumour and assist with vascular dissection. However, they were unable to differentiate the arteries and veins inside the kidney therewith reducing the practicality of the model. They

stress the necessity of improved vascular imaging for preoperative decision making in challenging procedures such as treatment of bWT with NSS. [46]

Wellens et al. (2019) performed a retrospective study to assess the added value of personalized 3D anatomical models in comparison with conventional imaging for the preoperative planning of NSS in paediatric patients. Six pediatric oncology surgeons and one pediatric urologist retrospectively assessed preoperative 2D conventional imaging data and subsequently assessed the corresponding 3D models visualized with both 3D printing and augmented reality. It was concluded that the 3D visualisation resulted in a significant improvement of the anatomical understanding for the renal artery, vein, tumour and urinary collection system. There was no significant difference between 3D printing and augmented reality. They showed that 3D visualisation can potentially help surgeons prepare for this intricate surgical procedure. Comparable with Girón-Vallejo et al, they state that improved imaging is essential for accurate and useful vasculature modelling as high quality imaging is at the base of the 3D visualisation. Additionally, automation of the segmentation process is required for the use of 3D anatomical models in clinical practice. [47]

In order to cope with the current limitations of imaging quality and segmentation process, a combination of semi-automatic segmentation algorithms that use the NC-MRA sequence visualizing the intraparenchymal arteries is proposed. The sequence may allow for an arterial-venous differentiation in a T2-W sequence to accommodate for robust vasculature 3D segmentation with crucial clinical information. Together with semi-automatic segmentation algorithms for the kidney, veins, urine collection system (UCS) and tumour, a complete 3D anatomical model of the WT patient can be constructed in a reproducible and robust manner. The arteries are one of the most important anatomical structures during NSS and the surgeon requires reliable information. Therefore, reproducibility, user-independence and robustness of the arterial model is crucial for the preoperative planning.

3DSlicer 4.10.0 (Kitware Inc, New York, USA) is a software package used for the development of 3D anatomical models [48]. It is an extensive open-source platform for medical image processing. It is used for general image segmentation and 3D modelling. However, anatomical model computation in 3DSlicer is difficult, user-dependent and time consuming. Therefore, research is required on more specific techniques to allow for validation and user-independence. Lupulescu et al. (2019) describe in their systematic review the limitations of data segmentation. Segmentation and post-processing can take multiple hours and it requires multiple software tools. [43] This limitation must be addressed for the clinical implementation of 3D anatomical models. In order to work within the current clinical

workflow, the 3D-modelling has to be fast, preferably within two hours.

There is a clear clinical need for improved imaging and visualisation techniques for the preoperative planning of Wilms tumour surgery. 3D visualisation is likely to increase the understanding of the relationship between relevant anatomical structures [47]. Reproducibly constructed and accurate 3D anatomical models based on imaging without additional adverse effects, contrast agents or radiation, can together assist the surgeon to decide upon the most optimal surgical procedure and increase the quality of life of WT survivors.

## 1.2 Research aim

For the preoperative planning of a WT patient, a paediatric surgeon requires 3D anatomical insight to understand the relationships between the tumour, kidney, urine collection system and vasculature. This insight is vital to prepare the surgical procedure; whether that is radical nephrectomy or nephron sparing surgery. We aim to evaluate the use of additional vasculature visualisation modalities and develop a segmentation algorithm which combinedly allow for reproducible and accurate 3D anatomical models for the preoperative planning of Wilms tumours surgery. The developed imaging and segmentation techniques have to be fast (within two hours) and anatomically representative.

### 1.2.1 Research questions

Two research questions were defined based on the two research objectives.

#### **Research questions:**

- What is the difference in the contrast-to-noise ratio from a NC-MRA sequence in comparison to the currently used CE-MRA sequence and how do both sequences and the T2-W sequence differ in arterial visualisation?
- What is the accuracy and model quality of the anatomical tumour and kidney 3D models resulting from a semi-automated MRI segmentation algorithm in comparison to a ground truth computed through 3DSlicer and how robust is the renal arterial segmentation algorithm?

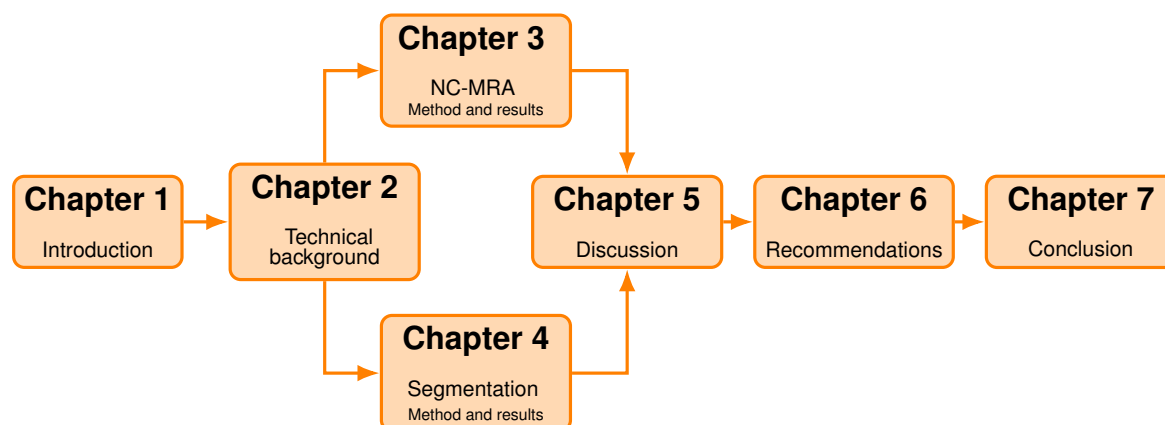


Figure 1.3: Schematic overview of the outline of this thesis.

## 1.3 Outline

The outline of the thesis is schematically illustrated in Figure 1.3. In the introduction, the clinical relevance and research aim are explained. Two major research themes for the preoperative planning for WT patients are described; a novel NC-MRA sequence for the visualisation of the intraparenchymal arteries and a semi-automatic segmentation algorithm for the 3D visualisation of the anatomy. In Chapter 2, the technical background of both the NC-MRA and the segmentation algorithm are described. In Section 2.1, we describe the basic principles behind the proposed sequence, the effect of multiple parameters on the expected image and how we optimized these parameters on adult volunteers previous to our study. In Section 2.2, the principles behind the different steps of the segmentation algorithm are explained.

Subsequently, Chapter 3 describes both the methods and results concerning the clinical implementation of the NC-MRA sequence. Patient inclusion criteria, parameter settings and a qualitative and quantitative evaluation are described. The methods and results regarding the semi-automatic segmentation algorithm are elaborated upon in Chapter 4. Again the patient inclusion criteria are explained together with a qualitative and quantitative evaluation. Additionally, we explain the use of virtual phantom and the robustness study. In the discussion in Chapter 5, both research subjects come together. Research questions are answered both through a technical and medical point of view. In Chapter 6, the short- and long-term recommendations are given and finally, the thesis is concluded in Chapter 7.



# Technical background and development

Both the NC-MRA and segmentation algorithm are based on techniques which are further explained in the following sections. These techniques are used to answer the previously described research questions. Additionally, we examined the most important parameters for the use of the b-SSFP sequence in the paediatric clinical MR protocol. The chosen parameters were determined in accordance with literature and a senior MR-operator. The semi-automatic segmentation is an elaborate combination of multiple segmentation techniques for the different anatomic regions.

## 2.1 Balanced Steady State Free Precession

Balanced Steady State Free Precession is a MR sequence previously applied, among others, for the visualisation for renal arteries. The main principle behind b-SSFP is achieved through a Repetition Time significantly shorter than the T2 relaxation time of the imaged tissue. Thus the residual transverse magnetization does not decay before the next excitation and at the next excitation, the longitudinal magnetization is added again. After multiple cycles, the combined longitudinal signal (free induction decay, T1 and T2\*-weighted) and the residual transverse magnetization (T2-weighted) reach a steady state. [49] This combined signal provides a mixture of T1- and T2-weighted imaging. This contrast makes it a valuable technique for renal vessel visualisation. The gradient-induced dephasing is nulled out through compensation with balanced gradients at every repetition [50]. Therefore the sequence is intrinsically flow independent in all three directions. The T2/T1-weighted signal combination of b-SSFP has a contrast which heavily depends on the flip angle (FA). At the right FA, liquids (e.g. blood) with a high T2/T1 ratio develop more signal in comparison to solid tissues (e.g. the kidney) with a low

T2 / T1 ratio. Additionally, in order to differentiate the blood signal into arterial and venous blood, an inversion pulse is added. The 180° inversion pulse and imaging delay (Inversion Time, TI) results in removal of outflowing venous blood, imaging of fresh inflowing arterial blood and saturation of the kidney. A saturation band is added to suppress signal from inflowing fresh venous blood from the inferior vena cava. Many parameters and settings influence the resulting image such as the TI, FA, slab positioning and renal motion compensation. Their contributions to the image quality are further explained below. Subsequently, we describe the optimization of sequence parameters during the testing on healthy volunteers and the results.

### Inversion time

The TI is the time between the inversion pulse and the start of the excitation. Figure 2.1 shows a schematic explanation of how the TI contributes to inflow enhancement. After the 180° inversion pulse, the longitudinal magnetization is negative within the volume of the pulse. The longitudinal relaxation starts going back to the original position along the positive axis, the speed of which is dependent on the T1 relaxation time of the tissue (visualized in green in Figure 2.1). The longitudinal magnetization  $M_z$  of the solid tissue after an inversion pulse is given in Equation 1. As can be seen in the equation, the magnetization depends on the waiting time  $t$  and the T1 relaxation time of the specific tissue.

$$M_z = M_o * (1 - 2 * e^{-t/T1}) \quad (1)$$

After the TI, the longitudinal relaxation in the kidney should be null, completely removing the signal coming from the kidneys. The b-SSFP sequence starts and due to the steady state, the magnetization of the saturated volume is constant from this point. As fresh unsaturated blood from the aorta above the inversion pulse volume flows into kidney, a high magnetization difference between arterial blood and the kidney results in visualisation of the arterial branches with fresh blood. Proper timing of the TI is crucial for the signal saturation of the kidney as the steady state of the b-SSFP sequence fixates the contrast once the imaging starts. If the TI is either too short or too long, the contrast between arterial blood and kidney is decreased as the magnetization of the kidney may not be completely nulled out. This technique is called inflow enhancement and ensures the inherent blood contrast of b-SSFP is differentiated between an arterial and venous signal.

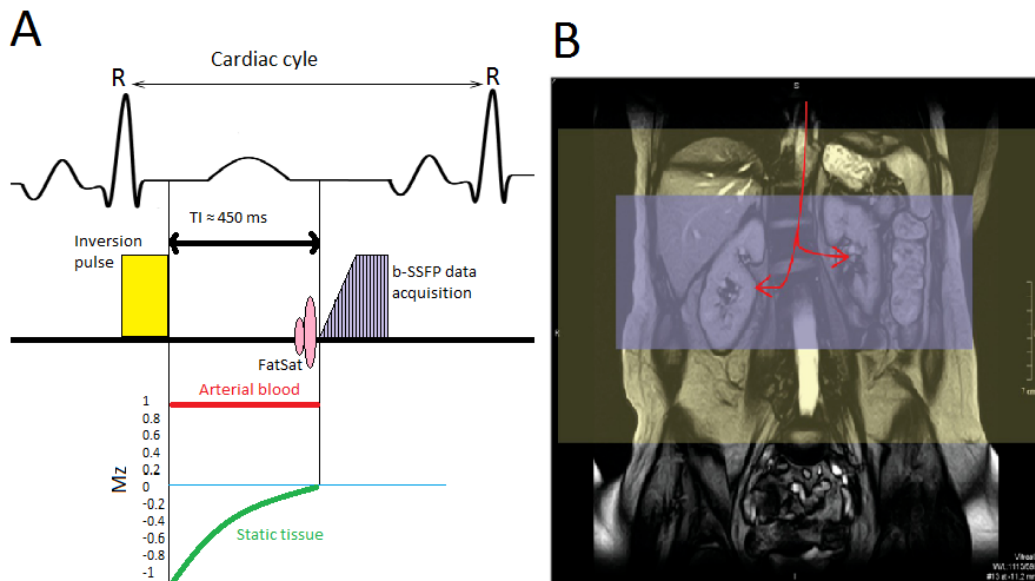


Figure 2.1: A = schematic explanation of the inflow enhancement. After the  $180^\circ$  inversion pulse, the longitudinal magnetization (Mz) for all tissues within the volume of the pulse (yellow) are negative. While waiting for fresh inflowing arterial blood (red), the Mz of the inverted volume starts restoring the equilibrium (green), the speed of which is dependent on the T1 characteristics of the tissue (Equation 1). At TI, the longitudinal magnetization in the kidney is null and the kidney will produce little or no signal. As the b-SSFP is a steady state, the magnetization will remain constant in the imaged Field of View (purple). Additionally, a fat saturation slab is added to saturate fat from the abdomen (pink). B = overview of the position of the FOV and inversion pulse. Adapted from McRobbie et al. 2017 [3].

## Flip Angle

If the FA is optimal, the T2 / T1 ratio of the tissue determines the signal intensity; given by the formula 2.  $M_{ss}$  is the steady state magnetization signal,  $M_0$  is the totally available magnetization and T1 and T2 are the relaxation times of the imaged tissue.

$$M_{ss} \approx \frac{1}{2} M_0 \sqrt{\frac{T_2}{T_1}} \quad (2)$$

Theoretically, the FA results in the optimal magnetization between  $70^\circ$  and  $90^\circ$  [50]. If the T1 relaxation time is roughly equal to the T2 relaxation, which is commonly the case for fluids, the resulting magnetization is approximately 50 % of the totally available magnetization. This is a particularly strong signal-to-noise ratio [50]. Tissues with a T1 longer than the T2 relaxation times thus have a lower magnetization at the same FA, which is true for solid tissue. Theoretically, the T2 can also be longer than the T1 relaxation time (maximal twice as long), resulting in an increased magnetization [51]. However, this is clinically irrelevant. In conclusion, an inherent contrast exists between fluids and solid components if the FA is set

correctly. Optimization of the FA is thus important to get the right contrast. However, blood flow and surrounding tissue may affect the T2 / T1 ratio and therefore the signal intensity. Additionally, with the added inversion pulse, we expect a low intensity of the kidney, regardless of the FA.

### **Slab positioning and FOV orientation**

As caudal fresh venous blood flows inside the FOV, the inferior vena cava is also visualized. In order to remove the inflowing venous blood from the image, a saturation band is added. The saturation band is positioned upstream of the inferior vena cava to cope with the flow as there is a slight delay between start of the saturation and the start of the data acquisition. However, it is unknown how far caudally this saturation band has to be positioned. Additionally, the direction of the FOV influences the visualisation of the arterial vasculature. A transverse FOV may allow visualisation of anterior-posterior and lateral-medial tumour-induced deformations of the arterial vasculature. However, a transverse FOV may limit the visualisation of the complete renal vasculature tree. A coronal view can improve appreciation of arteries situated more cranially or caudally.

### **Renal motion**

All sequences were cardiac triggered with an electrocardiogram to cope with artefacts resulting from pulsating vessels. The data acquisition takes place at end-diastole. However, the image quality is also influenced by renal motion, mostly caused by respiratory motion. Multiple techniques can be used to compensate for respiratory motion such as respiratory triggering, respiratory gating and respiratory tracking in combination with respiratory gating. With a respiratory trigger, the scan starts and stops at certain positions of the breathing pattern. The respiratory motion of a patient volunteer is measured with a bellow placed around the diaphragm. For a respiratory gate, the breathing motion is measured with a continuous dynamic 1D (pencil-beam) T1-W scan. This scan is positioned at the dome of the diaphragm and measures the movement of the diaphragm. The operator sets an upper and lower threshold. If the diaphragm is outside this window, the information scanned during this period is not used to complete the sequence. For respiratory tracking, the position of the FOV varies in the cranial caudal direction parallel to the current height of the diaphragm. Again the respiratory motion is measured through a pencil-beam T1-W scan.

### 2.1.1 Parameter examination on healthy volunteers

In the following paragraphs, we elaborate on the decision of different sequence parameters. A list of requirements was adhered to during the optimization of the sequence parameters. The list of minimal requirements was drafted in consultation with the radiology and surgery department.

- Visualisation: the extraparenchymal renal/segmental arteries
- Voxel size: 1 x 1 x 1 mm<sup>3</sup>
- Coil: anterior coil
- Motion compensation: cardiac and/or respiratory
- Breathing instructions: free breathing
- Field strength: 1.5 tesla
- Sequence dimensions: 3D and/or 4D
- Maximum scanning time: 5 min
- FOV: intraparenchymal renal artery branches (5 cm thick in the coronal plane)

Five healthy volunteers were enlisted for the parameter optimization. Imaging was performed on a clinically used 32-channel Ingenia 1.5 T MRI (Philips Medical Systems, Best, Netherlands) equipped with a gradient system with an amplitude of 45 mT / m and a max slew rate of 200 T / m / s. A 32-channel torso coil was used, the volunteers were positioned head first in a supine position. The healthy volunteers were all males with an average age of 24. We examined the Inversion Time (TI), Flip Angle (FA), saturation band position, FOV position and motion compensation technique. Additionally, coincidentally, one volunteer mimicked paediatric physiological parameters. This is addressed separately. All resulting images are shown as a transverse maximum intensity projections (MIP).

Four different inversion times were examined; the minimal ms (250 ms), 400 ms, 450 ms and the maximum ms (620 ms at a heart rate of 75 bpm). All other parameters were kept constant. The shortest possible TI is set to allow inflow of the arterial blood in the renal arteries. If the TI is shortened, the inflow of fresh arterial blood is reduced. When using a cardiac trigger, the maximum duration of TI is dependent on the heart rate as the duration of the sequence has to fit between two heart beats (fixed at 90 % of the R-R interval). 400 and 450 ms were chosen because they were in between the minimally and maximally allowed TI. The resulting images are shown in 2.2. As a TI of 450 ms appeared to completely saturate the magnetization in the kidney, it was empirically decided that 450 ms appears to be the optimal TI. If the signal is nulled at this TI, it means the T1 relaxation time is 650 ms (derived through Equation 1).

The same volunteer was scanned at two different FA's, 50° and 90°, to evaluate an increase of the FA. Results are shown in Figure 2.3. We did recognize an

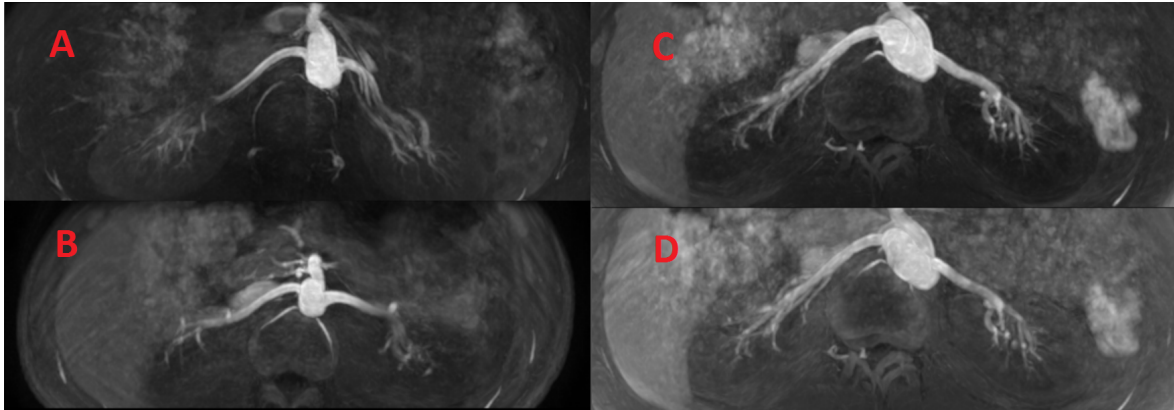


Figure 2.2: Four MIP b-SSFP scans with inflow enhancement at different settings of the Inversion Time (TI); A = 250 ms (min value), B = 400 ms, C = 450 ms, D = 620 ms (max value, 90 % of RR interval). C shows the preferred saturation of the kidney and delineation of the intraparenchymal arteries. In A, we can not fully appreciate the intraparenchymal segmental arteries due to insufficient inflowing fresh arterial blood. B and C show a good saturation of the kidney and adequate inflow of arterial blood.

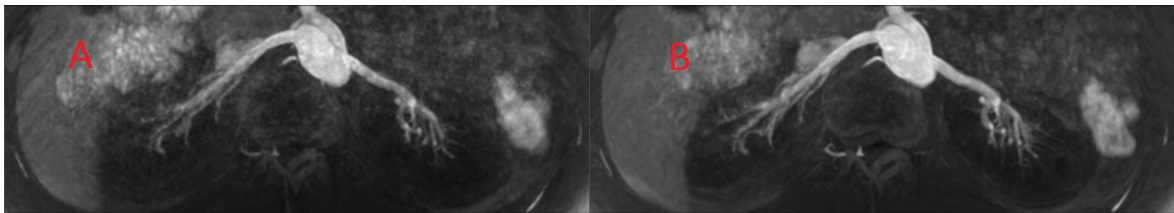


Figure 2.3: Two MIP b-SSFP with arterial inflow results of the same volunteer at a different FA; A = FA 50°, B = FA 90°; B shows a more homogeneous and slightly increased signal intensity in the renal arteries.

increased overall intensity at a higher FA, as was expected. Based on visual inspection, a FA of 90° shows an improved contrast of the renal arteries and is therefore used. This corresponds with Tan et al. (2012) (90°) and Katoh et al. 2004 (85°) [4, 52].

Three different positions of the saturation slab were tested. Additionally, both coronal and transverse FOV were evaluated. The first slab position was right below the lower pole of the kidney (position A), the second slab was positioned at a distance twice the slab thickness from the lower pole (position B) and the third position was a double slab below the lower pole of the kidney (position C). Additionally a coronal FOV (position D) was scanned. Results are shown in Figure 2.4. Position A showed an improved venous saturation in comparison to position B. The double slab positioning did not influence the signal intensity of the vena cava. The double slab does increase the Specific Absorption Rate of the patient (SAR, W / Kg), the absorption rate of electromagnetic radiation in the body. An increased SAR can lead to heating of the tissue and can possibly be dangerous. Therefore, it was decided that a double slab was unnecessary. The coronal FOV resulted in

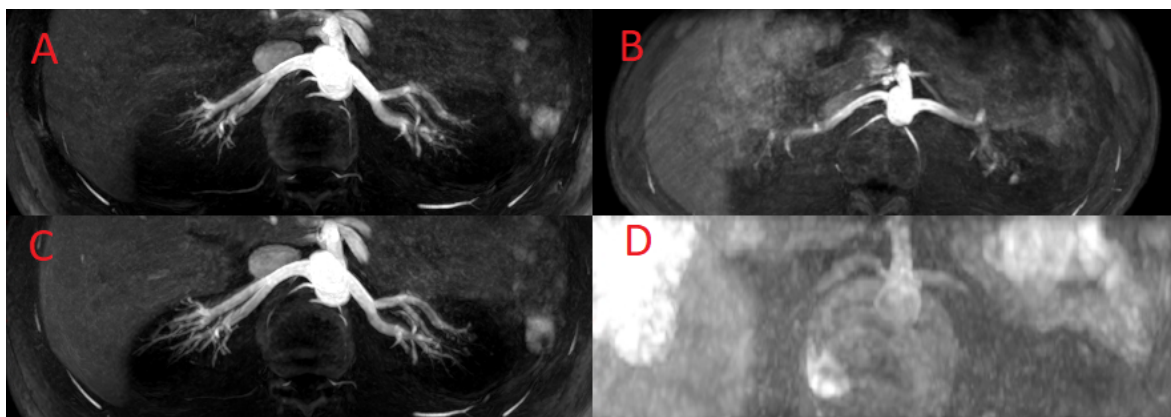


Figure 2.4: b-SSFP with arterial inflow with different saturation slab positions; A = saturation slab caudal of the kidney, B = saturation slab at a distance twice the slab thickness from the lower pole, C = a double slab caudal to the kidney, D = coronal FOV;

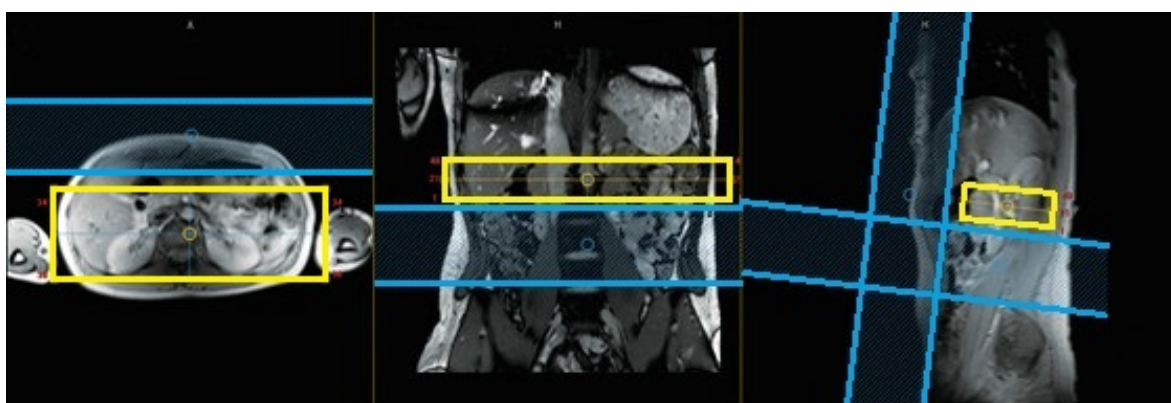


Figure 2.5: Overview of the saturation slab positions. The FOV (yellow) consists of 50 slices measuring 2 mm each. The reconstructed slice thickness is 1 mm, resulting in a sagittal thickness of 5 cm. The FOV is orientated parallel to the renal artery going towards the pathological kidney (not depicted). The inversion slab (blue) is situated right below the lower pole of the kidney. A saturation slab runs along the abdominal wall for fat suppression.

image artefacts. We did not take a further look at different FOV settings in the coronal plane. An overview of the saturation slab position A and FOV is given in Figure 2.5.

All three motion compensation techniques were tested on the same healthy volunteer. Respiratory gating showed the most preferred image quality, the arterial edges were more distinct in comparison to only cardiac triggering or respiratory triggering. The results of the different motion compensation techniques are shown in Figure 2.6. However, the scanning time increased significantly with respiratory motion compensation and visibility of the intraparenchymal branches did not appear to increase based on visual inspection. Respiratory tracking was considered unsuccessful, showing banding artefacts throughout the volume. This was most likely caused by the inability to keep up the steady state with a moving

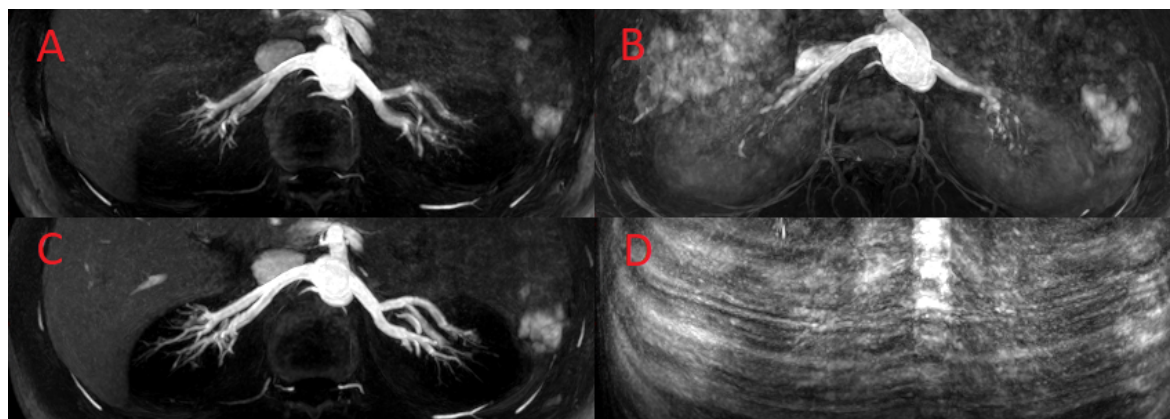


Figure 2.6: b-SSFP with arterial inflow with different motion compensation techniques; A = cardiac trigger, B = respiratory trigger, C = respiratory gate, D = respiratory gate and tracking; C shows a more homogeneous signal intensity in the renal arteries.

FOV. As the FOV varies, the protons shortly start to lose their relaxation position, interrupting the steady state. To conclude, respiratory motion compensation was deemed unnecessary for pediatric patients.

### Mimicking of the physiology of paediatric patients

Paediatric patients may require specific adjustments of the sequence parameters to cope with the expected change in physiology. Young children have a faster heart rate and a different breathing pattern. Coincidentally, one of our volunteers had a physiologic normal increased heart rate of 100 bpm which closely resembles the heart rate of our patient population ( $\pm 4$  years old). Furthermore, the breathing pattern was mimicked by making the subject breath faster during the scanning. This allowed an experimental setup which partially resembled the scanning of a paediatric patient.

The TI was adjusted to 400 ms as the 450 ms did not fit between the R-R interval. Patients in our age group have a mean heart rate of 100-120 bpm so adjustment of the TI for paediatric patients is expected. A respiratory trigger was added to compensate for the increased breathing speed. As expected we saw a slight decrease in saturation of the kidney and surrounding tissue due to the decreased TI. However, this was deemed clinically irrelevant as all intraparenchymal arteries were still visualized. Again, the respiratory trigger did decrease the blurring around the vessel wall. However, as the scanning time was longer, it was again considered unnecessary to add a respiratory motion compensation technique.

### Resulting sequence parameters

The settings of the most important parameters were determined for the b-SSFP sequence. The experiments showed the best contrast between intraparenchymal arterial branches and kidney parenchyma at a TI of 450 ms, FA of 90°, a cardiac trigger and a single saturation band placed caudally to the caudal kidney pole. The resulting image is shown in Figure 2.7. The FOV matrix size was approximately 260 \* 260 \* 50 with a voxel size of 1.15 x 1.15 x 2 mm<sup>3</sup> (reconstructed voxel size 0.56 x 0.56 x 1 mm<sup>3</sup>). The TR and TE are ± 7 and 3.5 ms, respectively. As discussed, the TI is subject to change as it depends on the heart rate of the paediatric patient. The total scanning time is between 3 and 5 minutes, which depends on the TI.

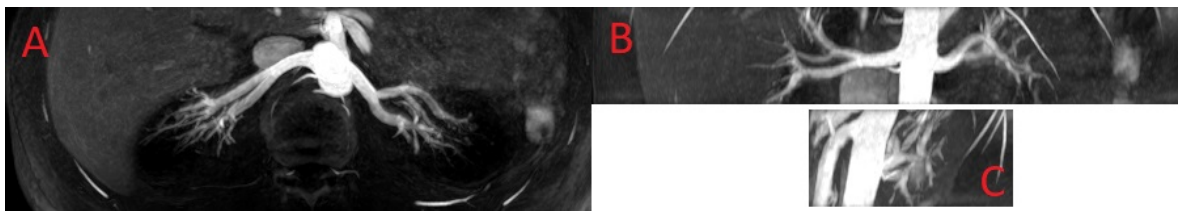


Figure 2.7: MIP b-SSFP scans with inflow enhancement of the same volunteer scanned with the resulting parameter settings; A = transverse plane, B = coronal plane, C = sagittal plane.

## 2.2 Development of a semi-automatic segmentation algorithm

Segmentation of the arteries, veins, UCS, tumour and kidney all require different techniques with or without manual input and with different pre- and post-processing filters. A combination of the available MRI sequences (T2-W, T1-W post-contrast, b-SSFP) was used to derive the complete anatomical model in MATLAB R2018b (MathWorks; Natick, Massachusetts, USA). The MR-sequences were combined through a rigid alignment algorithm based on the given Digital Imaging and Communications in Medicine (DICOM) information. This algorithm sets the individual DICOM images into the same coordinate system. The coordinate system of the T2-W sequence is used due to FOV encompassing the entire abdomen and the high transverse in-plane spatial resolution. Further explanation and MATLAB code of the rigid alignment can be found in Appendix C. The user provides clinical information such as the region of interests (ROI), the amount of tumours and the tumour location (left and/or right). The results of the segmentations are saved as a stereo-lithography (.STL) file with the appropriate anatomical colour. The different elements in the algorithm are schematically visualized in Figure 2.8. The following subsections illustrate the techniques behind the used segmentation algorithms for

the different organs.

### **Image filtering**

In the algorithm, a combination of pre-and post-processing filters are used. An anisotropic diffusion filter and vessel enhancement filter are used for the pre-processing. The vessel enhancement filter is further explained in Subsection 2.2. The anisotropic diffusion filter is used for the filtering of the T2-W sequence at the start of the vein segmentation. This decreases the leakage of the region growing algorithm as explained in Paragraph **Vein segmentation**. It is also used to increase the homogeneity of the intensity and strengthen the edges of the kidney in the T1-W post-contrast sequence to improve the result of the watershed computation (Paragraph **Kidney segmentation**). The filter mainly acts as a Gaussian filter, therewith blurring the area. Additionally, the Gaussian filter is combined with an edge seeking function which allows the filter to stop at these edges. Therefore, the bigger areas of the image are smoothed, without altering the important edges.

Additional to the pre-processing filters, multiple post-processing filters are used to further smooth the segmentation and increase the model quality. A dilation filter is used to increase the size of the arterial segmentation. This allows for an improved visual representation of the arterial model. A Gaussian filter is combined with a dilation filter to smooth the manual correction of the tumour segmentation. An erosion filter is applied to the vein segmentation to slightly reduce the size of the active contouring result.

### **Artery segmentation**

The segmentation section of the algorithm starts with the development of the 3D arterial model. The b-SSFP sequence is used as an input for the segmentation of the aorta, renal artery and the extra- and intraparenchymal segmental branches. The proposed image filter and segmentation algorithm was based on the work of Technical Medicine student M. Brasz [53]. The user determines the volume of interest (VOI). An enhanced Frangi-filter is used to enhance the contrast of the vessel structures [54, 55]. The enhanced Frangi-filter is a tubular filter of varying sizes which searches for tubular structures inside the VOI. The Frangi-filter has two main parameters;  $\sigma$  and  $\tau$ . The parameter  $\sigma$  is the "radius" of the Gaussian tubular structure, whereas  $\tau$  controls the output uniformity. The resulting filtered image with enhanced vascular contrast is segmented through fuzzy c-means clustering [56]. This segmentation technique designates every pixel of the volume into two or more clusters (segments) based on similarity measures. These measures can be

intensity, distance and connectivity. The enhanced volume is segmented into two clusters, resulting in an arterial segmentation and the background. The arterial segmentation is manually checked on wrongful segmentations and, if necessary, corrected before the 3D anatomical model is computed from the binary volume. Attachment of the inferior vena cava on the arterial segmentation has to be manually removed.

### **Vein segmentation**

Firstly, the FOV of the b-SSFP sequence is aligned on top of the transverse T2-W and is used as the FOV for the vein segmentation. This eliminates any input from regions outside of the arterial FOV. The arterial segmentation is used as an overlay to distinguish the vascular structures in the T2-W sequence. The veins appear black in the T2-W sequence, due to intravoxel phase dispersion, whereas the arteries are now white. Secondly, the user manually determines the background once in every four slices. A "Box" interpolation is used to fill the background back the original size. A "Box" interpolation averages pixel values within the specified cuboid shape. Thirdly, the user determines the foreground with a region growing algorithm [57]. The user is asked to determine a seed point inside the veins which initializes the region growing algorithm. The algorithm increases the size of the seed point by one pixel, therewith creating a region. The value of each neighbouring pixel is then compared to the mean of the current region. If the value of a pixel is within the tolerance level of the current mean, it is added to the region. The tolerance level is set at 0.04, which is a very narrow tolerance to limit leakage outside the veins. The user determines the foreground once in every three slices and the remaining slices of the volume are segmented with an active contouring algorithm [58]. The foreground grows every iteration of the algorithm and aims to minimize the amount of "energy" necessary to grow. The foreground grows towards vascular borders and continues between the slices ultimately filling in the entire venous structures. The active contouring algorithm iterates 4 times based on the method of Chan-Vese [59]. Due to leakage at the vascular walls, manual correction of wrongly segmented anatomy is typically required to complete the vein segmentation. For example, due to equal intensities of the vena cava and the liver, the active contouring algorithm might leak into the liver if this was part of the background.

### **Urine collection system segmentation**

The VOI of the kidney in the T2-W sequence is manually determined for segmentation of the urine collection system (UCS). At the start of the algorithm, the user is asked to answer questions on relevant clinical information. Based on the

patients pathology (uni- or bilateral), the algorithm runs once or twice. Also, the user has to define the amount of tumour locations. The urine inside the collection system typically has a bright signal intensity in T2-W image and is easily identified if the patient has a sufficiently full collection system. However, as the collection system may not be filled or compressed by the tumour, visualisation and therefore the segmentation of the UCS remains difficult. The ureter, pyelum and calcyxes are segmented with the region growing algorithm. Again the user defines an initial seed point and the algorithm computes the region. A tolerance level of 0.04 is used. The user determines the seed point for every slice of the VOI and may stop whenever there is no UCS left to segment.

### **Tumour segmentation**

The tumour VOI is determined by the user in the fat-suppressed T1-W post-contrast sequence. A canny edge detection filter is used to roughly detect the pseudocapsule which exists in most WTs [60, 61]. The "edge filtered" image is closed, a dilation followed by an erosion, to determine the rough segmentation. The user is asked to manually correct the segmentation in every slice to correct for leakage and undersegmentation. The algorithm is an adaption of the earlier work of Technical Medicine student M. Buser [62]. As the tumour aspect is particularly heterogeneous, the tumour VOI in the fat-suppressed T1-W post-contrast sequence is not rigidly registered with the T2-W sequence to cope with the "inter-sequence" displacement. Instead, the transform matrix used for the intensity-based rigid registration of the kidney is also used for the registration of the tumour. The tumour algorithm reiterates depending on the amount of tumour localization's. The computed 3D tumour models are all saved under a different name and are not combined into one model. This allows further handling of the individual models.

### **Kidney segmentation**

To conclude the segmentation section of the algorithm, the kidney is segmented based on the fat-suppressed T1-W post-contrast sequence. This sequence has a homogeneous intensity of the kidney with clear borders, arising from the GBCM. The previously determined VOI of the UCS segmentation is also used for the kidney VOI. The VOI in the T1-W post-contrast sequence is registered with the T2-W to compensate for patient movement with an intensity-based "multimodal" rigid registration algorithm from MATLAB. For the segmentation, the user defines a ROI in the kidney in one slice. The mean intensity of the ROI is used to determine the foreground in the total volume through a threshold with an empirically

determined intensity range [mean intensity -0.05, mean intensity +0.05]. The foreground is extended 10 mm in all three directions to determine the background. Additionally, the tumour is added to the background to ensure the tumour-kidney border is correctly segmented. A watershed algorithm finds the kidney border and segments the kidney volume. It determines the edge between the foreground and the background based on the gradient of the intensity. The resulting kidney volume is smoothed with a Gaussian filter. Again, this algorithm runs for both the left and right kidney if the patient has bilateral disease.

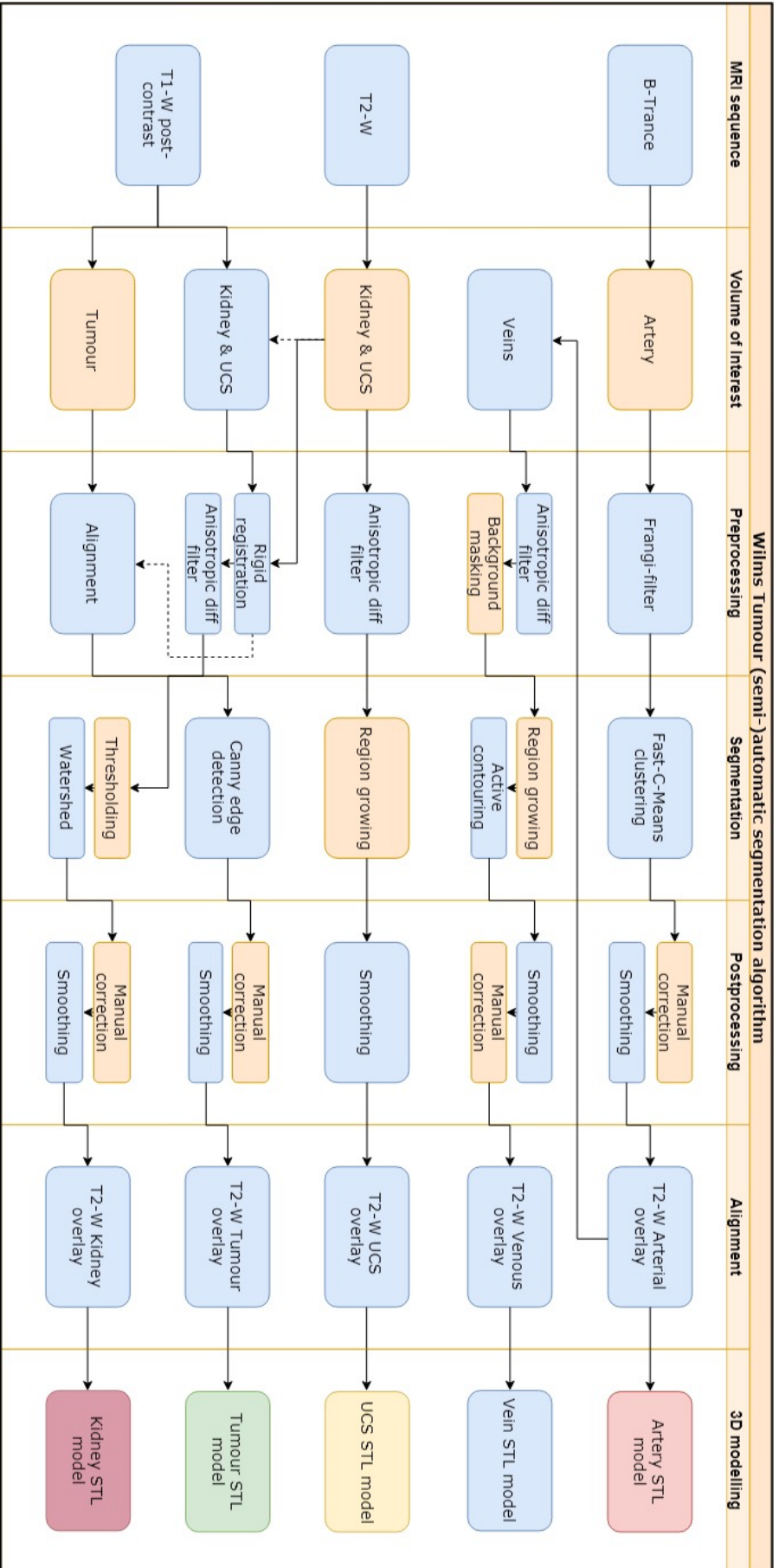


Figure 2.8: Complete schematic overview of the developed Wilms Tumour segmentation algorithm. The algorithm comprises of seven elements per model: the MRI sequence, Volume of Interest (VOI), pre-processing, segmentation, post-processing, alignment of the model segmentation and the creation of the 3D model. The blue boxes are automated algorithms; orange boxes are manual procedures; the colours in the 3D modelling box represent the actual colour of the 3D model. Filled lines are regular steps, the dotted lines visualize additional alignment steps. Prior to the tumour segmentation, the kidney VOI is determined in the T1-W sequence and this is rigidly registered with the kidney VOI in the T2-W sequence. The transformation matrix derived from the rigid registration is used to align the tumour VOI with the T2-W sequence.

# NC-MRA implementation and evaluation

Using the parameter settings described in Section 2.1, the non contrast-enhanced magnetic resonance angiography sequence was evaluated through a prospective pilot study. In the coming chapter, the methods and results of this pilot study are discussed.

## 3.1 Methods

We aimed to include seven patients to scan with the optimized b-SSFP MRA sequence. Patients were selected by the surgery department of the Princess Máxima Center for Pediatric Oncology, Utrecht, the Netherlands between April 1, 2019 and June 1, 2019. Paediatric patients of all ages suspect for a renal tumor were included if they received a diagnostic 1.5 or 3 T MRI or if they received a MRI for preoperative planning and/or response evaluation. Patients had to be scanned according to the standard kidney tumour protocol. Patients whom were scanned with a kidney tumour protocol but were suspect for a Neuroblastoma were excluded.

The standard paediatric kidney tumour protocol is performed on a 1.5 T system (Achieva; Philips Medical Systems, Best, Netherlands). First a coronal 3D T2-W sequence is scanned, followed by a fat-suppressed T1-W sequence, DWI sequence (b values of at least 0 s / mm<sup>2</sup>, 100 s / mm<sup>2</sup> and 1,000 s / mm<sup>2</sup>) and a fat-suppressed T2-W MultiVane sequence. Before injection of the contrast bolus, the b-SSFP sequence is scanned. Subsequently, the GBCM (Gadovist; Bayer Pharma, Berlin, Germany) was administered intravenously at a dose of 0.1 mmol / kg body weight. The scanning operator proceeds with the 4D CE-MRA when the contrast enters the descending aorta. Finally, an additional fat suppressed T1-W post-contrast sequence is scanned.

The patients were intravenously administered Hyoscine butylbromide (Buscopan; Boehringer Ingelheim, Bracknell, UK) with a dose of 0.4 mg / kg body weight with a maximum of 5 mg for children < 6 years and a maximum of 10 mg for children < 10 years in order to reduce bowel peristalsis. All FOVs were set by the scanning operator except for the b-SSFP sequence, which was set by a technical physician. If the patient did not receive the aforementioned MR scans, the patient was excluded from the quantitative and qualitative NC-MRA analysis.

The patients were scanned with a TI of 450 ms. If 450 ms was not possible, the technical physician chose the value based on the maximally allowed TI (90 % of the R-R interval). The heartbeat used for the cardiac trigger was measured preferably with a three-lead electrocardiogram (ECG) or else with a Physiological Pulse Unit (PPU). The transverse FOV was set parallel to the renal artery of the pathological kidney in the coronal view in the T2-W sequence and encompassed the complete intraparenchymal arterial branch. The FOV in the coronal plane contained 50 slices with a reconstructed size of 1 mm. The saturation band was positioned below the lower pole of the kidneys.

The b-SSFP scans were analysed through a qualitative and quantitative evaluation. The quantitative evaluation was performed through a self written algorithm in MATLAB.

### 3.1.1 Quantitative evaluation

The b-SSFP and the CE-MRA of the included seven patients were assessed quantitatively through the method of Tan et al. (2012) [4]. They describe a method to quantify the contrast-to-noise ratio (CNR, equations 3 and 4) in renal MRA coronal MIP images. The mean signal intensity (SI) is measured in regions of interest (ROI): the renal and intraparenchymal segmental artery (RA; SA), kidney parenchyma (KP), tissue around the renal artery (TRA) and paravertebral muscle (PV). These rectangular ROI's have to have the same size in both images of the same patient. We deploy the same method in transverse MIPs. First, the user determines the 3D volume which has the highest intensity at the aorta and renal artery in of the 4D volume. The resulting 3D volume is then spatially aligned with the NC-MRA as described in Appendix C to ensure both the CE-MRA and NC-MRA have the same matrix dimensions. Subsequently, both transverse MIPs (2D) are translationally registered based on the intensity to correct anatomical movement between the sequences. An example of the CE-MRA and NC-MRA alignment and registration is given Figure 3.1. The assessor determines the position of the rectangular ROI in both the NC- and CE-MRA, making sure the positions roughly

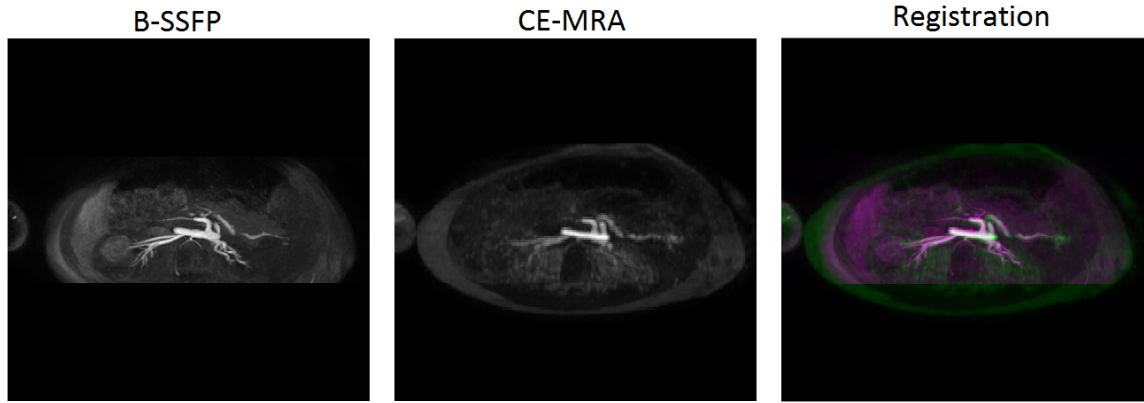


Figure 3.1: Result of the alignment and translational registration of the CE-MRA (moving) with the b-SSFP sequence (fixed) of patient 1. The left image is the resulting transverse MIP from the NC-MRA (b-SSFP). The figure in the middle shows the transformed CE-MRA and the right figure visualizes the result after spatial alignment and translational registration. Areas in white have the same intensity after registration; areas in green and magenta have different intensities, which is expected outside of the vasculature.

match in both MIP images. The CNR of the renal artery is defined as:

$$CNR_{RA} = \frac{SI_{RA} - SI_{TRA}}{STD_{PV}} \quad (3)$$

and the CNR of the intraparenchymal segmental artery is defined as:

$$CNR_{SA} = \frac{SI_{SA} - SI_{KP}}{STD_{PV}} \quad (4)$$

The paired students T-test was used to analyze the the CNR of the renal artery and intraparenchymal segmental arteries on both the NC- and CE-MRA sequences. A p - value < 0.05 was considered significant.

### 3.1.2 Qualitative evaluation

One experienced paediatric radiologists (A.L.) assessed the image quality of the arterial vasculature in the b-SSFP, the CE-MRA and the T2-W sequence. We also evaluated the image quality of the vasculature of T2-W sequence as this sequence is currently used to assess the intraparenchymal vasculature. The quality of the aorta (segment I), main renal artery (segment II), extra- and intraparenchymal arteries (segments III and IV) were subjectively scored based on a 4-point scale as described by Klee et al. (2012) [33].

1. bad image quality, renal vasculature is not visualized and images can not be used for preoperative planning;
2. problematic image quality, low image resolution resulting in poor visualisation of the vasculature and artefacts;

3. adequate image quality for preoperative planning, minor artefacts with no decreasing image quality in the relevant vasculature;
4. excellent image quality, depiction of all renal vasculature with no artefacts.

The results were analyzed with a Wilcoxon Signed Rank test to analyze the difference in image quality for every vasculature segment. A  $p$  - value  $< 0.05$  was considered significant.

## 3.2 Results

Seven WT patients were scanned with the b-SSFP sequence as described in section 2.1. All patients had unilateral disease. One patient had bilateral nephroblastomatosis (NB) with a uWT lesion nested inside the NB (patient 3). The average age was  $4.5 \pm 2.4$  years old. One patient underwent the MR examination for diagnosis (patient 2a), 6 patients were scanned for a preoperative response evaluation. One patient had previously had a nephrectomy (patient 5). Patient 2 was scanned both for diagnostic purposes (2a) and preoperative response evaluation (2b). An overview of the patients parameters is given in Table 3.1. For logistic reasons, one patient was scanned on a 3T MRI (patient 4). One patient was not scanned according to paediatric kidney tumour MRI protocol (patient 6). Both patients were excluded from further qualitative analysis as the scanned CE-MRA sequence is not equal to the other patients.

The average scanning time was 3 minutes and 52 seconds, the average heart rate  $111.4 \pm 11.1$  bpm and the average TI was  $389 \pm 42.1$  ms. All seven transverse MIPs of the b-SSFP sequences are shown in Figure 3.2.

### 3.2.1 Quantitative evaluation

Five of the resulting b-SSFP scans were successfully quantitatively assessed through measuring the CNR of the renal artery and CNR of the intraparenchymal segmental artery. The results of the quantitative analysis are shown in the quantitative evaluation section of Table 3.2. The FOV of 2 patients did not encompass the paravertebral muscle (patients 1 and 2a). The paravertebral muscle was used as a baseline measurement for the standard deviation of the intensity. It was decided that the air could be used instead.

The average CNR of the renal artery in the b-SSFP sequence was  $192.8 \pm 69.7$ . The average CNR of the renal artery in the CE-MRA sequence was equal to  $234.1 \pm 67.8$ . The b-SSFP sequence of 4 out of 5 patients had a lower CNR of the renal artery in comparison to the CE-MRA sequence. However, there was no significant difference in the CNR of the renal artery between the b-SSFP MRA and CE-MRA

Table 3.1: Overview of the clinical and scan parameters of 6 different patients. ECG = three-leads electrocardiogram; PPU = Physiological Pulse Unit. Patients are in chronological order.

Patient	Tumour type	Reason for MR	Gating tool	Age (years)	Heartrate (bpm)	TI (ms)	Scan time (min:s)
1	uWT Right	Preoperative	PPU	4	115	375	3:00
2a	uWT Right	Diagnostic	ECG	8	100	400	4:00
3	Bi- NB	Preoperative	ECG	3	120	360	3:30
4	uWT Left	Preoperative	ECG	4	130	320	3:45
5	Wilms	Preoperative	PPU	3	100	420	3:30
2b	uWT Right	Preoperative	PPU	8	105	450	4:50
6	uWT	Preoperative	PPU	1.5	110	395	3:40
Mean				4.5	111	389	3:45
STD				2.4	10	39	

with a p - value of 0.668. The average CNR of the segmental arteries in the b-SSFP sequence was  $189.2 \pm 77.3$ . The average CNR of the segmental artery in the CE-MRA sequence was equal to  $110.8 \pm 112.1$ . The b-SSFP sequence now did show an increase in CNR in 4 out of 5 patients in comparison to the CE-MRA sequence. However, again, there was no significant difference in the CNR of the intraparenchymal segmental artery between the b-SSFP sequence and CE-MRA with a p - value of 0.068.

Visually, there is a clear increase in CNR of the renal and segmental arteries with the b-SSFP sequence. Figure 3.3 shows a comparison of the coronal MIP images of the b-SSFP sequence and CE-MRA in the same FOV. The CNR of the different anatomic regions and different sequences are plotted in Figure 3.4. Here we appreciate the difference in contrast between the different sequences more evidently. Measured in the CE-MRA sequence, the mean CNR over the length of the artery has dropped and the standard deviation has increased. However, the mean CNR and standard deviation in the b-SSFP sequence remain consistent over the course of the artery. In only patient we see an increase in CNR in the intraparenchymal segmental arteries in the CE-MRA sequence compared to b-SSFP.

### Qualitative evaluation

The radiologist scored four vasculature segments based on a 4-point scale in the b-SSFP, CE-MRA and standard T2-W sequence. Mean scores are reported in Table 3.2. There was no difference in visualisation of segment I between the b-SSFP sequence and T2-W. However, according to the results derived with a

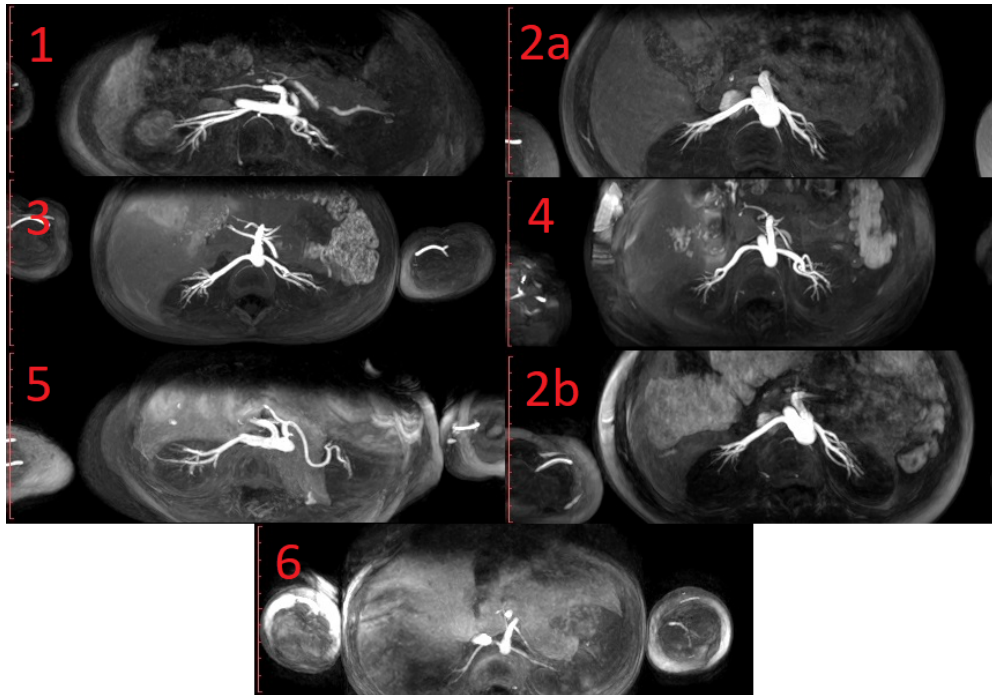


Figure 3.2: The transverse MIP images resulting from the implementation of the b-SSFP with arterial inflow sequence of seven Wilms Tumour patients. All patients had unilateral disease, except for patient 3 whom had a bilateral tumor. The MIPs clearly visualize all four arterial segments. Patient 5 had previously had a nephrectomy. Therefore, the only remaining renal artery is shown. In patient 2 and 6, the inferior vena cava can be appreciated.

Wilcoxon Signed Rank test, there was a significant difference between the b-SSFP and CE-MRA sequence in the visualisation of all segments ( $p < 0.05$ ;  $< 0.04$ ;  $< 0.04$ ;  $< 0.03$ ). The b-SSFP clearly improves the visualisation of the important arterial vasculature of the kidney in comparison to the CE-MRA. There was no significant difference between the NC-MRA and the standard T2-W sequence in the visualisation of segments I and II ( $p = 1$ ;  $< 0.4$ ). However, there was a significant difference between the two sequences in the visualisation of both segments III and IV ( $p < 0.03$ ;  $< 0.04$ ). There is a clear overall improvement of the extra- and intraparenchymal arteries with the b-SSFP sequence. The radiologist notes that the NC-MRA sequence improves the understanding of the intrarenal vasculature. It helps to differentiate the venous and arterial vasculature at a high resolution which is considered difficult on the standard T2-W sequence.



Figure 3.3: Two coronal MIP images of the same patient (2a); left is the b-SSFP sequence and right is the CE-MRA sequence. Visually, there is an increase in contrast of the b-SSFP sequence at the level of the renal and segmental arteries in comparison to the CE-MRA.

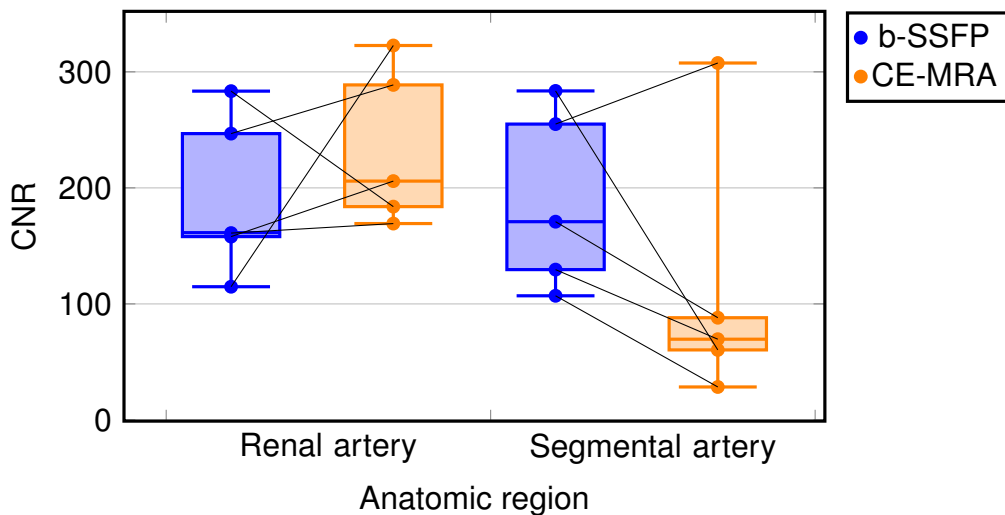


Figure 3.4: Results from the quantitative evaluation of the b-SSFP sequence (blue) and the CE-MRA sequence (orange). The contrast-to-noise ratio (CNR) was derived through an adjusted method described by Tan et al. (2012) [4]. The CNR was measured at the level of the renal artery and at the intraparenchymal renal arteries in aligned transverse MIP images. The connected dots represent the same patient.

Table 3.2: Results of the quantitative and qualitative evaluation of the optimized b-SSFP sequence. The mean CNR of the renal (RA) and intraparenchymal segmental arteries (SA) are shown in the quantitative segment. In the qualitative segment, the mean score and one standard deviation as assessed by the radiologist is given for the different vasculature segments; the aorta (segment I), main renal artery (segment II) and the extra- and intraparenchymal arteries (segments III and IV).

#### Quantitative evaluation

	b-SSFP	CE-MRA	p - value
CNR RA	$192.8 \pm 69.7$	$234.1 \pm 67.8$	0.668
CNR SA	$189.2 \pm 77.3$	$110.8 \pm 112.1$	0.068

#### Qualitative evaluation

	b-SSFP	CE-MRA	T2-W
Segment I	$4 \pm 0$	$3.25 \pm 0.4$	$4 \pm 0$
Segment II	$4 \pm 0$	$2.5 \pm 0.5$	$3.8 \pm 0.4$
Segment III	$4 \pm 0$	$1.25 \pm 0.4$	$3 \pm 0$
Segment IV	$3 \pm 0$	$1 \pm 0$	$1.6 \pm 0.5$

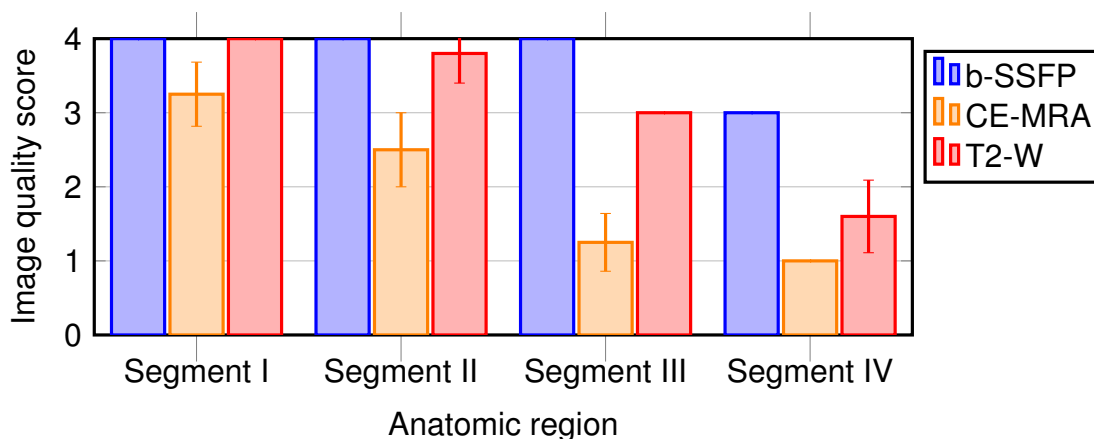


Figure 3.5: Results of the qualitative assessment of three MR sequences used for vasculature imaging; b-SSFP (blue), CE-MRA (orange) and T2-W (red). The radiologist scored four vasculature segments based on a 4-point scale; the aorta (segment I), main renal artery (segment II), extra- and intraparenchymal arteries (segments III and IV). The mean score is giving with 1 standard deviation.

# Implementation and evaluation of the segmentation algorithm

The 3D models resulting from the developed segmentation algorithm described in Section 2.2 were evaluated through a retrospective pilot study. The methods and results of this pilot study are further described.

## 4.1 Methods

The MRI scans of 7 patients were retrospectively segmented and used for the evaluation of the segmentation MATLAB algorithm. All MRI scans were used anonymously. If the patient did not undergo the required MRI scans (T2-W, fat-suppressed T1-W post-contrast and the b-SSFP sequence), the patient was excluded from the evaluation. The models were evaluated through comparison with 3D anatomical models computed with 3DSlicer by a technical physician.

3DSlicer was used to produce 3D anatomical models which were regarded as a ground truth. There was no standardized procedure for this computation. Many of the used techniques are user dependent and require anatomical knowledge and personal judgement. The b-SSFP sequence was segmented through a threshold technique to compute the 3D arterial models. Wrongfully segmented areas were manually removed with a "scissor" in the 3D viewer. Subsequently, this segmentation was used as an overlay in the T2-W sequence to differentiate between arteries and veins inside the kidney. The region growing algorithm was used to segment the intraparenchymal veins, renal vein and vena cava. Likewise, the UCS was segmented with the region growing algorithm. The kidney and tumour segmentation are derived with a watershed algorithm. The user manually determines areas of the tumour, kidney and background in the T1-W post-contrast sequence. This is done once in every three to four slices. The watershed algorithm then computes the tumour and kidney border. Many different filtering algorithms

were used for the computed segmentations. A "joint smoothing" filter was used to smooth the kidney, tumour and background segmentation together. This filter smooths the border between the different segmentations. Additionally, Gaussian and manual smoothing of the segmentations are used based on the opinion of the assessor.

First the optimal arterial segmentation algorithm parameters ( $\sigma$  and  $\tau$ ) were determined through segmentation of a virtual phantom. These parameters were used for the development of the 3D anatomical models of the patients. Subsequently, the results from the 3DSlicer computation and the MATLAB segmentation algorithm were quantitatively and qualitatively assessed. The tumour and kidney results were quantitatively compared. The robustness of the arterial segmentation was assessed to evaluate the robustness and reliability. The complete 3D anatomical models resulting from both procedures were qualitatively scored on the model quality. Both the quantitative and qualitative evaluation are further explained.

#### 4.1.1 Parameter determination

In order to quantitatively determine the right values for the parameters  $\sigma$  and  $\tau$ , a virtual phantom of paediatric renal arteries was computed. The phantom of the renal arteries was derived from a high resolution CTA. 3DSlicer was used to segment the CTA with a threshold segmentation technique and manual removal of any artefacts. The virtual phantom was considered representative because it was based on the CTA scan of a 5 year old WT patient who had no compression of the arteries. Even though the CTA has a smaller pixel size compared to the b-SSFP sequence ( $0.08 \times 0.08 \text{ mm}^2$  smaller in the transverse plane), this should not affect the developed MATLAB arterial segmentation algorithm. The segmentation algorithm was used to segment the virtual phantom with different parameter values for the vessel enhancement filter ( $\sigma$  and  $\tau$ ). The results were scored and quantitatively assessed with the DICE coefficient (Equation 5). DICE coefficient is an overlap based metric, measuring the overlap of the segmentation results (SR) and the ground truth (GT) ranging from 0 to 1. The DICE coefficient can be seen as the ratio of overlap between two volumes. The DICE is defined as

$$DICE = \frac{2 * |SR \cap GT|}{|SR| + |GT|}. \quad (5)$$

The resulting  $\sigma$  and  $\tau$  values were used for the subsequent segmentation of the NC-MRA sequences of our patient study.

### 4.1.2 Quantitative evaluation

The patient anatomical models were computed both through the developed segmentation algorithm and 3DSlicer. The DICE coefficient was used to assess the overlap of the tumour and kidney volumes. The arteries, veins and UCS were not quantitatively evaluated due to the variability in the computation of the 3DSlicer models. For example, in 3DSlicer, no VOI was used to determine the arterial segmentation. Instead, the complete b-SSFP sequence is segmented and manually corrected in 3D with a "scissor" tool. This results in a vastly different VOI of the 3DSlicer segmentation compared to the MATLAB segmentation and therefore, the DICE coefficient is not a representative parameter. This can be observed in Figure 4.1, \*; the left renal artery of the arterial model is smaller in A (MATLAB segmentation result) compared to B (3DSlicer segmentation result).

Furthermore, the arterial segmentation algorithm was quantitatively assessed through a reproducibility measurement. The artery model was computed for every patient three times by the same assessor with a minimum of two days in between the computations. The time interval was set to minimize remembrance of the previously computed model. The mean DICE was measured per patient between all three artery models. The mean overall DICE coefficient was used to evaluate the robustness. A DICE coefficient  $> 0.9$  was considered robust, this means that the algorithm produces comparable arterial models for the same patient over time. The results from the venous and UCS segmentation algorithms were only assessed qualitatively.

### 4.1.3 Qualitative evaluation

The 3D anatomical models from the MATLAB algorithm and from 3DSlicer were qualitatively scored based on a 4-point scale indicating whether the 3D anatomic models results are realistic and accurate.

1. completely unrealistic and inaccurate models, unfit for preoperative planning;
2. slightly unrealistic representation, information is false/lacking, low usability;
3. realistic representation but certain information is false/lacking, usable;
4. realistic and accurate representation of the anatomy/pathology, no false or lacking information, high usability.

The assessment was performed using the 3D visualisation software of 3DSlicer for both anatomical models (resulting from MATLAB and 3DSlicer). Five anatomical models were assessed; arteries, veins, UCS, tumour and kidney. Again a Wilcoxon Signed Rank test was used to evaluate the difference in model quality of the different

anatomic regions between MATLAB and the 3DSlicer segmentation result. A  $p$ -value  $< 0.05$  was considered significant.

## 4.2 Results

Six patient specific anatomical models were successfully computed through a newly developed semi-automatic segmentation algorithm and 3DSlicer. One patient (pat 5) was unintentionally not scanned according to the kidney tumour MR protocol. Therewith, the patient was not scanned with the required standard sequences to compute 3D anatomical models with the MATLAB algorithm. Furthermore, the FOV was incorrectly set and only encompassed half a kidney. However, this patient was scanned with the proposed NC-MRA sequence and therefore we were able to compute 3D arterial models. These were used for the quantitative robustness evaluation. A comparison of the results computed with the MATLAB segmentation algorithm and computed with 3DSlicer anatomical model is shown in Figure 4.1. The  $\diamond$  illustrates the FOV of the NC-MRA. As the FOV of the b-SSFP sequence is set parallel to the renal artery, the aorta is sliced with an angle equal to the angle of the renal artery. Subsequently, the FOV is used as an overlay on top of the T2-W sequence to construct the vein anatomical model. Thus the cut-off of the vena cava is within the FOV of the MRA. The  $\star$  shows the difference in VOI of the arterial model between the MATLAB arterial algorithm and 3DSlicer. The left renal artery is longer and more extensive in the model computed with 3DSlicer. Also, in 3DSlicer, the mesenteric artery is removed through the "scissor" application. Finally, the  $\bullet$  visualizes the observer-variation between the two segmentation techniques. It appears that the tumour protrudes from the kidney in A, unlike in B it appears enclosed by the kidney.

### 4.2.1 Quantitative evaluation

A binary virtual phantom of renal vasculature was segmented with the artery segmentation algorithm. The evaluation showed a DICE coefficient of 0.897 at a  $\sigma$  of 2 and a  $\tau$  of 0.5. The resulting DICE coefficients at different values for  $\sigma$  and  $\tau$  are shown in Figure 4.2. A mean DICE coefficient of 0.897 is considered an excellent representation of the virtual phantom. Visual inspection of the result shows an underestimation of the virtual phantom by approximately one pixel. This is expected; the tubular structure of the Frangi-filter has a Gaussian shape. As the shape of the filter iterates through the virtual phantom, the filter stops at the binary border. Due to the Gaussian filter, the filtered result has a sharply increasing intensity across the artery. During the segmentation, the filtered result becomes

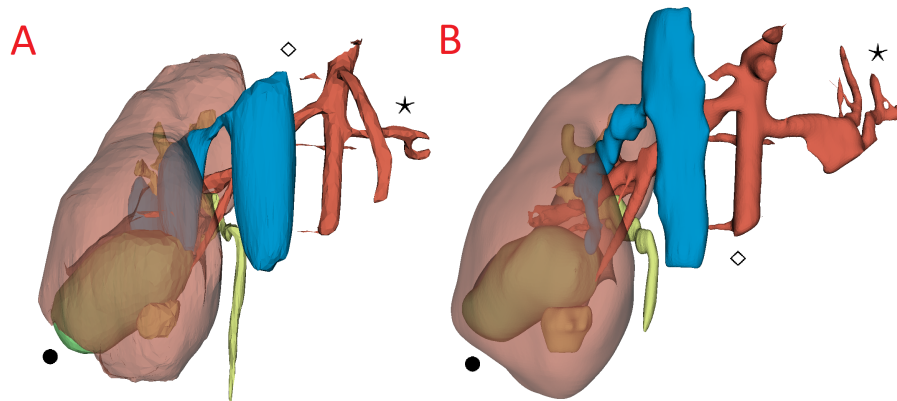


Figure 4.1: 3D anatomical models computed through the developed MATLAB segmentation algorithm (A) and derived with 3DSlicer (B) of patient 1. The  $\diamond$  illustrates the FOV of the NC-MRA, set parallel to the renal artery. The  $\star$  shows the difference in VOI of the arterial model between the MATLAB arterial algorithm and 3DSlicer. The  $\bullet$  visualizes the observer-variation between the two segmentation techniques.

binary again and the Gaussian shape is cut off, causing a slight undersegmentation. This is expected not to be the case during the segmentation of the renal NC-MRA scans. As the intensity of a real NC-MRA vessel is not binary but also has a sharply increasing intensity, the shape of the filter has a better "fit" on the vessel.

The mean DICE coefficient was determined between the segmentation of the tumour and kidney resulting from 3DSlicer and the developed algorithm. The mean DICE coefficient for the tumour was  $0.79 \pm 0.06$ , the mean DICE coefficient for the kidney was equal to  $0.83 \pm 0.05$ . The results are visualized in Figure 4.3. Noteworthy, the tumour DICE coefficient of patient 2a (0.79) and 2b (0.68), whom were scans from the same child, appear to decrease of time. The first scan was a diagnostic scan, whereas the second preoperative scan was after six rounds of chemotherapy. As the MATLAB algorithm and user delineate based on the T1-W post-contrast sequence, which is commonly used to distinguish vital and necrotic tissue, this appears to give an underestimation of the tumour volume.

To measure the reproducibility of the developed MATLAB arterial segmentation, NC-MRA scan was segmented three times by the same assessor. Subsequently, the DICE coefficient was measured between all three results. The results of the reproducibility measurement are shown in Table 4.1. The DICE coefficient was determined between the first and second segmentation (GT 1, SR 2), first and third segmentation (GT 1, SR 3) and second and third segmentation (GT 2, SR 3). The mean overall DICE coefficient was  $0.94 \pm 0.04$ . The DICE coefficient is not expected to be exactly 1, as the user determines a ROI which may be different for every computation and the user can correct the result. The mean DICE of  $0.94 \pm$

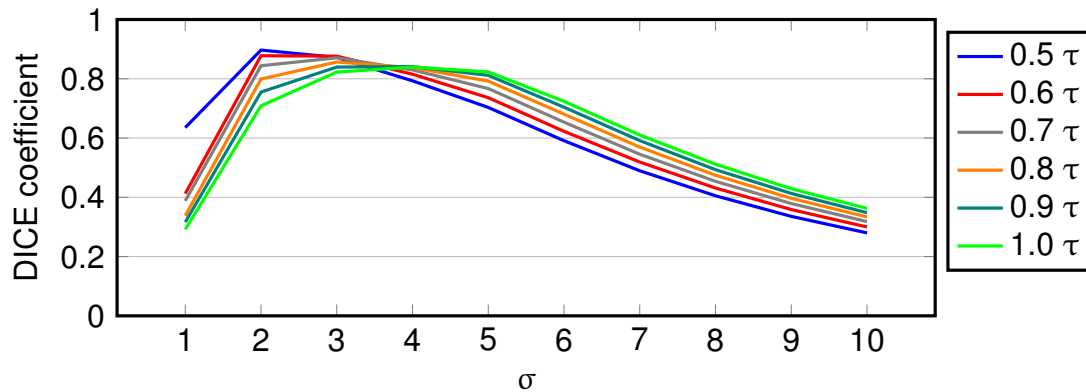


Figure 4.2: Results of the quantitative virtual phantom study. The DICE coefficient was measured between a binary virtual phantom and the segmentation algorithm result. The DICE coefficient was computed for different settings of  $\sigma$  and  $\tau$  in the arterial segmentation algorithm. The parameters  $\sigma$  and  $\tau$  are used to control the Frangi-filter;  $\sigma$  is the "radius" of the Gaussian tubular structure and  $\tau$  controls the output uniformity. A  $\sigma$  and  $\tau$  of respectively 2 and 0.5 showed the highest DICE coefficient (0.897).

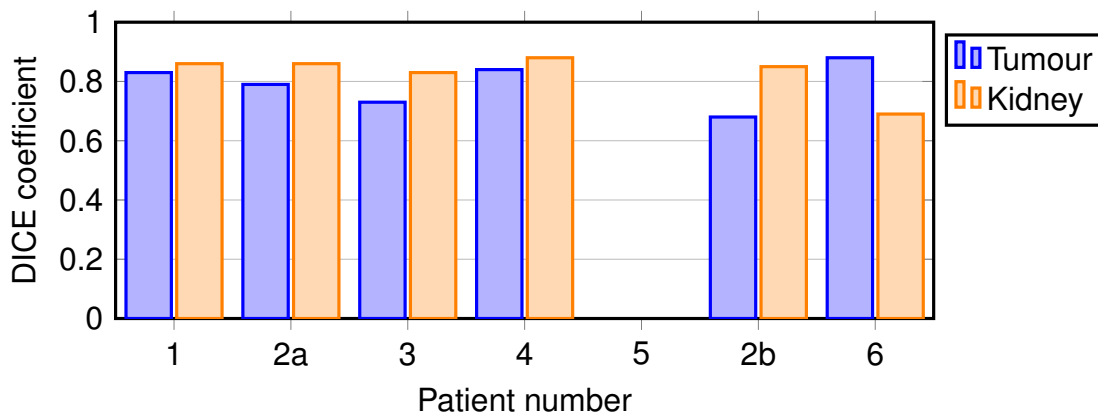


Figure 4.3: Results of the quantitative evaluation of the tumour and kidney segmentation. The DICE coefficient was computed for the tumour (blue) and kidney (orange) segmentations resulting from the MATLAB segmentation algorithm and 3DSlicer. The DICE coefficients are given for the included seven patients. Patient 5 did not undergo the right sequences and FOV to complete the segmentation through the developed MATLAB algorithm.

0.04 indicates the arterial segmentation is robust and shows limited influence from the manual input by the assessor.

### 4.2.2 Qualitative evaluation

The image quality of the anatomical models from the MATLAB segmentation algorithm and the 3DSlicer computation were assessed based on a 4-point scale. The results are shown in Figure 4.4. The mean score of the arterial MATLAB result was  $3.83 \pm 0.41$ , the mean score of the arterial 3DSlicer model was equal to  $3.33 \pm 0.52$  ( $p = 0.083$ ) The vein 3D models of the MATLAB segmentation scored  $1.67 \pm 0.52$ , the mean score of the 3DSlicer result was equal to  $2.83 \pm 0.98$  ( $p = 0.038$ ). The urine collection system models derived with the MATLAB algorithm scored on average  $1.33 \pm 0.52$ , whereas the models computed with 3DSlicer scored a mean quality score of  $2.17 \pm 0.98$  ( $p = 0.102$ ). The tumour and kidney models from the MATLAB algorithm both scored  $3.5 \pm 0.55$ . Computed through 3DSlicer, both the tumour and kidney models scored  $3.67 \pm 0.52$ , ( $p = 0.564$ ,  $p = 0.317$ ).

*Table 4.1: Results of the quantitative reproducibility measurement. The DICE coefficient is given between three segmentations derived from the arterial segmentation algorithm at three different moments. The GT is the result which is considered the ground truth, SR is the result it is compared with.*

Patient Number	DICE GT 1 SR 2	DICE GT 1 SR 3	DICE GT 2 SR 3
1	0.99	0.89	0.89
2a	0.94	0.95	0.98
3	0.85	0.86	0.98
4	0.97	0.97	1.00
5	0.99	0.93	0.94
2b	0.92	0.92	0.97
6	0.96	0.90	0.91
Average	$0.95 \pm 0.05$	$0.92 \pm 0.03$	$0.95 \pm 0.04$

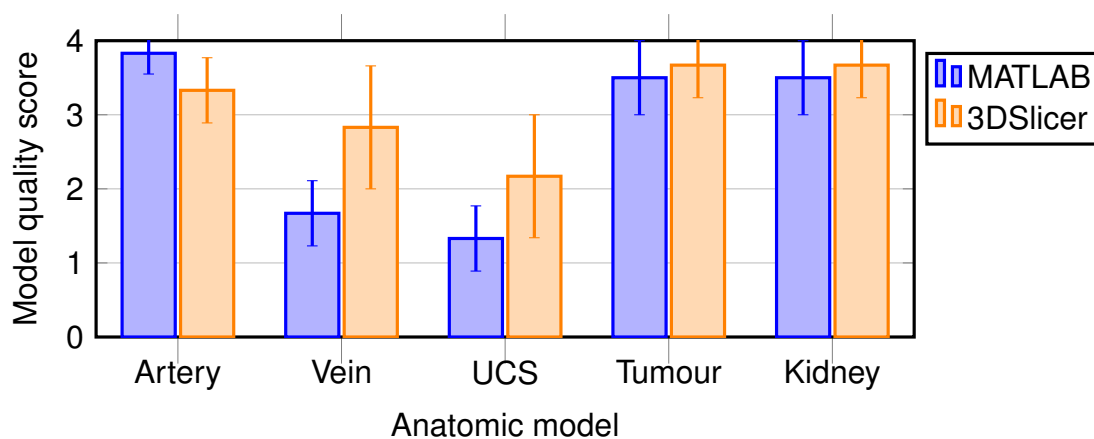


Figure 4.4: Results of the qualitative assessment of two segmentation techniques for the anatomical modelling of WT patients; computed through a developed MATLAB segmentation algorithm (blue) and 3DSlicer (orange). The models were scored on a 4-point scale. The mean score is giving with 1 standard deviation.

# Discussion

In this study, three dimensional visualisation techniques were improved and developed to assist during the preoperative planning of patients with a Wilms Tumour. For this purpose, a combination of a newly introduced MRA sequence and a developed segmentation algorithm were used to develop 3D anatomical models.

We successfully evaluated a NC-MRA sequence for the visualisation of intraparenchymal arteries in children with WTs. The inflow enhanced b-SSFP sequence showed an improved image quality of the intraparenchymal arteries in comparison to the T2-W and CE-MRA sequences according to a radiologist. Additionally, the CNR of the intraparenchymal arteries appeared to be, even though insignificant, higher in the b-SSFP sequence in comparison to the CE-MRA. The NC-MRA is devoid of contrast and radiation, robust and non-invasive. It is considered to have a visualisation quality matching CTA scans. The department of Pediatric Surgery at the Princess Máxima Center for pediatric oncology regards it as reliable, of significant value and safe to implement into clinical practice.

Additionally, a semi-automatic segmentation algorithm for the anatomical modelling of the arteries, veins, UCS, tumour and kidney of WT patients was developed. The scans resulting from the b-SSFP sequence were used for the differentiation of arteries and veins in the high resolution isotropic T2-W sequence. The results of the segmentation of the virtual phantom proved that the artery segmentation algorithm computes accurate 3D arterial models. Moreover, the quantitative assessment of the robustness of the arterial algorithm resulted in a high overall DICE coefficient with a small standard deviation. This assessment proved that the proposed technique (combination of the NC-MRA sequence and the MATLAB algorithm) is a reliable and user-independent technique for the 3D visualisation of the renal arterial vasculature. The proposed combination was considered vital to the improvement of the preoperative planning of patients with Wilms tumours [47].

The comparison of the 3D anatomical tumour and kidney models resulting from

the segmentation algorithm and the anatomical models computed with 3DSlicer showed that the MATLAB algorithm resulted in reliable kidney and tumour models. Both anatomical models computed with the MATLAB algorithm were high in quality with a score of  $3.5 \pm 0.55$  out of 4. Even though manual correction of leakage remains required, the anatomical models are insignificantly different from the computations with 3DSlicer. This was confirmed with a quantitative evaluation of the models through the computation of the DICE coefficient with an average of  $0.79 \pm 0.06$  for the tumour models and  $0.83 \pm 0.05$  for the kidney models. Both the qualitative and quantitative evaluation suggest that the developed 3D tumour and kidney models are representative.

## 5.1 Balanced Steady State Free Precession

The results of the proposed b-SSFP sequence were assessed both quantitatively and qualitatively. The qualitative evaluation showed that the average image quality of the b-SSFP sequence was considered good in WT patients. The small intraparenchymal segmental arteries (segment IV) were visualized with an image quality score of  $3 \pm 0$  out of 4. This is an improvement in comparison to the results from Klee et al (2012), who showed an average quality score of  $2.3 \pm 1.1$  for the intraparenchymal arteries in healthy children [33]. The improved image quality may be attributed to the difference in observers or the increased transverse resolution. Klee et al. scanned with a reconstructed voxel size of  $1.1 \times 1.1 \times 1 \text{ mm}^3$  whereas our proposed sequence has a reconstructed resolution size of  $0.56 \times 0.56 \times 1 \text{ mm}^3$ . This increased transverse resolution likely improved the visualisation of these intricate vessels. This resolution was essential for our specific purpose, visualisation of intraparenchymal arteries for the preoperative planning of patients with Wilms tumours. The comparison of results shows that the increased resolution was beneficial but the required increase in scanning time and may not be required for more general purposes.

The quantitative evaluation did not show a significant increased CNR of the renal and intraparenchymal arteries (CNR  $192.8 \pm 69.7$ ;  $189.2 \pm 77.3$ ) in the b-SSFP sequence in comparison to the CE-MRA sequence (CNR  $234.1 \pm 67.8$ ;  $110.8 \pm 112.1$ ). As the CE-MRA uses GBCM's to obtain a high CNR of the arteries, the comparable CNR of the b-SSFP sequence confirms that the technique used in b-SSFP is efficient. The difference in magnetization between low (blood) and high (solid tissue) T1 / T2 ratio's at a flip angle of  $90^\circ$  of the b-SSFP combined with an inversion pulse is a valuable technique to visualize vasculature. We did not find a significant difference in CNR between both sequences at the intraparenchymal arteries. This insignificance may be attributed to the small patient

population ( $n = 5$ ) for this analysis. Visualized in Figure 3.4, we can appreciate the trend of the CNR over the course of the artery. Here it is visualized that the b-SSFP appears more stable, with an improved mean and a smaller standard deviation in CNR of the intraparenchymal segmental artery. For four out of five patients, the b-SSFP sequence showed an improved CNR. For the fifth patient, the CE-MRA had an improved CNR yet the clinical value of this increase is minimal. This was already observed by Katoh et al. (2004) [52]. They also performed a direct comparison of a slab selective b-SSFP sequence and a (3D) CE-MRA sequence. The CNR of the b-SSFP sequence proposed by Katoh et al. (2004) was significantly superior to the CNR of the CE-MRA in both the renal artery and intraparenchymal segmental artery. B-SSFP implementation is still expected to have a significant improvement in CNR of the intraparenchymal arteries, a study with a bigger patient population will quantify this difference.

The results of the b-SSFP sequence were limited by the determination of the Inversion Time. The TI is the most important parameter as the effect of the TI is twofold; the waiting time after the  $180^\circ$  inversion pulse allows the longitudinal magnetization of solid tissue to go to null and gives time for the venous blood to flow away from the kidney. In adults, the 450 ms showed good saturation of the kidney and of the venous signal. We were able to scan with a TI of 450 ms on only one patient (patient 2b). Especially if the used TI is determined during a relatively quiescent period, the max TI might not fit between two heart beats when the heart rate of the patient increases. The sequence is thus forced to skip a beat. This was the case in patient 2b and explains the increased scanning time. There was a relatively low average TI (388.6 ms) and large standard deviation of  $\pm 10\%$  showing that a more specific rationale behind the TI might be required to decrease the deviation. A decreased deviation means the saturation of the solid tissue will be more consistent and the scanning time will decrease. Following Equation 1, lowering the TI down to 375 ms will increase the maximally obtainable signal in the kidney by  $\pm 10\%$ . When we take the signal loss into account, a lowered TI will not impact the image quality significantly, however the CNR might slightly decrease as there will be more signal coming from the kidney.

Both the quantitative (despite being insignificant) and qualitative evaluations appear to agree that the NC-MRA sequence improves the visualisation of the intraparenchymal arteries. The sequence is compliant to all the earlier described requirements, including the reconstructed voxel size. To conclude, the b-SSFP sequence is a robust and GBCM free sequence and may be used in clinical practice for the appreciation of the delicate arterial vessels inside the kidney of a Wilms Tumour patient.

## 5.2 Development of the segmentation algorithm

We evaluated the MATLAB algorithm results by comparing them with 3D anatomical models computed with 3DSlicer. The results of the 3D tumour and kidney models were quantitatively assessed and resulted in high average DICE coefficients.

Arguably, the 3DSlicer anatomical models may not be regarded as a ground truth as the current method has not been validated and the models are considered an approximation of the anatomy. However, the use of anatomical models from 3DSlicer is justifiable, as the specific true anatomical volumes may be less relevant to the preoperative planning of WT patients. The relationships between the different anatomical structures are more meaningful. These relationships depend strongly on location and direction, more so than the actual volume. Location and direction are visualized and segmented adequately through 3DSlicer thus giving an overview of the anatomy. The comparison of both techniques was used particularly to show how the semi-automatic algorithm compared to the shape and location. Therefore, it was decided that the resulting anatomical models of 3DSlicer could be regarded as ground truths for our analysis of the kidney and tumour. However, it remains important to realise that this comparison only gives an estimation of the accuracy of the models.

Both in MATLAB and 3DSlicer, anatomical modelling of a post-neoadjuvant chemotherapy Wilms Tumour remains challenging. The developed MATLAB algorithm uses an edge detection technique to segment a gross volume and additional manual correction allows further delineation of the tumour. An edge detection was chosen to identify the encapsulation of the tumour. Because heterogeneity of the tumour on MR, manual correction remains required for every slice despite of the algorithm used [63]. Manual correction is a subjective and tedious task, especially in patients with high volume tumours. Noteworthy, manual delineation of the tumour area seems indecisive. Müller et al. (2019, unpublished) segmented before and after neoadjuvant chemotherapy tumours in 2D T2-W MRI's and saw a difference in the volume of post-chemotherapy tumours of roughly 25 % with a high standard deviation of  $\pm 35$  % [63]. This high standard deviation caused by interobserver variability illustrates the difficulty of this task. They also noticed a dramatic increase in the interobserver variability between pre- and postchemotherapy delineations. This is expected to be caused by the difficult differentiation of necrotic and vital tissue. Thus, even with manual delineation, computing anatomically correct 3D tumour models remains elusive and difficult. Further work on more automated approaches for the segmentation of Wilms Tumour is required to obtain truthful, faster and user-independent segmentations.

The current 3D anatomical models derived with the MATLAB segmentation

algorithm do not visualize the veins and UCS accurately enough with a quality suitable for clinical use. Both anatomical models showed poor results during the qualitative visual assessment with a mean model quality score of  $1.67 \pm 0.44$  and  $1.33 \pm 0.44$ , respectively. We noticed a significant difference between the 3DSlicer and MATLAB vein models ( $p = 0.038$ ). Overall, the venous segmentation results were low in model quality, partially due to difficult assessment of the T2-W sequence. The venous system appeared difficult to delineate because of compression of the vessels and overall low visibility. In the MATLAB algorithm, the proposed combined region growing and active contouring segmentation algorithm leaks at the border of the inferior vena cava which requires post-processing filters and manual correction. However, the significant difference in comparison to the venous models derived with 3DSlicer may not be all attributed to the proposed algorithm. In 3DSlicer, the venous model is an interpretation by the assessor of the vasculature in the T2-W and NC-MRA sequence. In the proposed MATLAB algorithm, the FOV of the arterial segmentation is used as a FOV in the T2-W sequence. This eliminates any false-positive input. So even though the model quality of the MATLAB algorithm might be significantly lower, it may be more anatomically truthful. Additionally, as the venous anatomy can be, partially, derived from the arterial model, it is clinically less important.

Despite that some of the results of the developed MATLAB segmentation algorithm were not of adequate high quality and still require manual input, the overall result does allow a valuable clinically relevant appreciation of the anatomy. The described workflow of the alignment algorithm, pre- and post-processing filters, rigid registration algorithm and segmentation algorithms visualize the different relationships required for NSS.

### **5.3 Clinical implications**

The combination of a contrast-free MRA technique and segmentation algorithm resulted in 3D anatomical models with a previously unobtainable accuracy without the use of radiation. The NC-MRA sequence assists in the visualisation of the arteries with a high resolution. The increased image quality of the intraparenchymal arteries in the NC-MRA sequence in comparison to the T2-W sequence allows for an improved visualisation of the clinically crucial tumour-artery relationship. The 3D anatomical models computed through the segmentation algorithm allow for appreciation of the size and relationships of the anatomy and underlying pathology.

A clearer understanding of the tumour size, location of the mass, relationship with the vessels and UCS through improved imaging and 3D anatomical modelling may allow an improved insight on when to operate sparingly. Current guidelines on

NSS remain unclear and are heavily dependent on the opinion and skill of the surgeon. Murphy et al. (2018) review their experience with NSS for bWT patients in the St. Jude Children's Research Hospital [64]. Despite managing to safely perform NSS in 90 % of the patients, they emphasize the difficulty of the assessment of preoperative imaging. There are no well-defined criteria which help with the preoperative determination on feasibility of NSS. Currently, intraoperative delineation of the tumour and finding the tumour volume is the most difficult section during NSS. Ultrasound is commonly used for the intraoperative determination of the dissection plane. Even with intraoperative ultrasound, figures between 15.7 % to 31 % of the tumour masses treated with NSS which had positive margins have been reported [22, 65]. Unfortunately, upstaging as a consequence of a positive margin necessitates radiation and possibly additional chemotherapy [26]. 3D anatomical models may help surgeons to better understand when to operate sparingly and minimise the risk of positive margins. Additionally, it might give more insight on where and how these positive margins occur.

In a retrospective qualitative study on the use of 3D anatomical models for WT patients it was confirmed that these models improved the understanding of the anatomy and pathology between paediatric oncology surgeons [47]. However, the construction of the models was limited by the obtained image quality, inconsistent timing of the administered contrast bolus, the required input from medical specialists and required time for the manual segmentations. The first prospective study (unpublished) on paediatric 3D anatomical modelling was also limited by the low quality imaging [66]. We addressed these limitations through a collaboration of imaging and semi-automatic segmentation techniques. The high quality NC-MRA does not require timing by the operator, simply because there is no GBCM to administer. This sequence ensures a visualisation of the intraparenchymal arteries and prevents the use of an additional CTA. Subsequently, no medical specialist is needed to assist during the segmentation the intraparenchymal vasculature. This approach allows us to visualize more (intraparenchymal arteries), in a faster manner.

A combination of specific imaging and more automated segmentation algorithms might also improve the models derived with the venous segmentation algorithm. The imaging may be easily implemented with an different application of b-SSFP for MRVenography (MRV). B-SSFP is a sequence with inherent blood contrast. Combining it with an inversion pulse and imaging delay results in the MRA. However, removing the inflow enhancement should result in a sequence visualizing the complete vasculature. Subsequent subtraction of the inflow enhanced b-SSFP sequence results in a NC-MRV. The additional scanning time will be short considering there is only a cardiac trigger and no inversion time. This

"unenhanced" technique may also be useful in the volumetric assessment of a venous tumour thrombus [67]. Especially the length of the venous involvement of a thrombus is interesting to visualize because thrombosis are difficult to resect yet important to treat surgically [68].

The UCS anatomical models both from MATLAB and 3DSlicer showed a low model quality ( $1.33 \pm 0.52$  and  $2.17 \pm 0.98$ , respectively) due to poor visualisation in the T2-W sequence. Compression and discharge of the UCS can make it difficult for the assessor to recognize the calyces, pyelum and ureter. For some patients, it was hardly possible to segment the UCS in both segmentation techniques due to the poor visualisation, especially for kidneys with more centrally located tumours (e.g. patient 6). For these anatomical structures, novel imaging techniques may speed up segmentation and result in more robust 3D anatomical models.

The tumour-UCS relationship appeared difficult to derive through anatomical modelling, indicated by the low average quality of both the MATLAB and 3DSlicer anatomical models of the UCS, yet it is important during NSS. Rupture of the UCS can increase the risk of bleeding, urinoma or hydronephrosis and these patients may require additional surgical interventions [69]. Aldrink et al. (2018) saw urine leakage in 19 % of the kidneys treated with NSS [70]. Improvement of the UCS anatomical model is expected to allow for a better understanding of the UCS and decrease complications. However, more specific imaging techniques for the UCS may be required. Static-fluid MRUrography (MRU) can be used to visualize the UCS. This technique uses urine as a contrast agent in a heavy T2-weighted sequence [71, 72]. It is a fast, free-breathing protocol but requires a filled UCS. Morin et al. describe a MRU preparation by hydrating children intravenously with 10 mL / kg saline prior to the scan combined with diuretics and a bladder catheter [73]. Even though most patients have intravenous access to administer preoperative chemotherapy, this technique might be considered unreasonably invasive. The advantages of such an additional sequence have to be balanced with the patient hinder.

We have shown that a combination of high resolution MRAs and semi-automatic segmentation algorithms allows the creation of accurate 3D arterial models. Therefore, such a combined approach can be extended to create other anatomical models faster, more accurately and to increase the robustness of the segmentation result. Specific imaging techniques may speed up the process as the segmentation of these images is technically less demanding and can more easily be automated. Currently manual input is required to find the relevant structures of the veins and UCS which was proven to be difficult and inconsistent. Combining the aforementioned specific sequences with specialized algorithms allows the user to segment the structures more automatically and eliminate the use of manual input.

With the implementation of these techniques, we expect a better insight on when to operate sparingly, we expect an improved understanding of the positive margins seen during NSS and we expect increased intraoperative knowledge of tumour volume and the surrounding anatomy.

# Recommendations

Based on this work, we recommend two short-term and four long-term research objectives regarding the NC-MRA sequence, segmentation algorithm and clinical implementation.

## 6.1 Short-term

To further improve the application of b-SSFP, we must consider a more practically suited and protocolized parameter value of the Inversion Time. Currently, it is set at 450 ms and if this is not possible, the technical physician decided on a TI empirically. As the 450 ms was too high for our mean heart rate ( $111 \pm 10$  bpm), the baseline TI may be lowered to 375 ms which is slightly lower compared to our mean TI of  $388 \pm 39$  ms. Additionally, if the TI remains too long, the operator may deduct the TI by steps of 25 ms. The CNR of the image might reduce slightly as the magnetization of the surrounding tissue is not completely nulled out. However, the overall usability will not be jeopardized. Other parameters should be set as described in the technical background, Section 2.1 on page 11.

The second short-term recommendation is the improvement of the model quality of the veins and UCS resulting from the MATLAB segmentation algorithm. The models do not have a model quality required for clinical use. The vein and urine collection system models were scored as unusable and the kidney segmentation was scored as representative yet containing wrong information. This was recognized as both an algorithm and an imaging limitation. To improve the anatomical models of the veins and UCS, the proposed combination of MRV/MRU sequences and relatively easily implemented segmentation algorithms can provide accurate anatomical models. MRV and MRU are well described techniques and it should be feasible to use during the preoperative assessment after a brief pilot study on volunteers.

## 6.2 Long-term

On the long-term, we recommend using the non-contrast enhanced MRA technique described in this study not solely for renal MRAs. It has also been previously described for the use over MRPortography (MRP) and MRV of the liver [74]. Currently, a four phase CT scan is usually made to assess the liver arteries, portal vein and liver veins in paediatric patients with liver malignancies. However, timing of the bolus injection remains difficult, especially in the younger population [75]. The four phase CT is operator-dependent and if failed, the patient has received futile radiation and contrast agent. The surgeon can no longer use the CT for the preoperative planning as the relationship between the hepatic vasculature segments and tumour localization determines the proposed surgical procedure. Using the b-SSFP sequence for MRA/MRV/MRP of the liver may abolish the required four phase CT. However, this has not yet been performed in children. In order to overcome the problems of hepatic four phase CT's, a pilot study can be preformed to assess the feasibility of MR hepatic vasculature imaging in children.

Secondly, it is recommended to increase the automation of the Wilms Tumour segmentation algorithm. The current tumour segmentation protocol is based on a canny edge detection filter and manual correction. For the purpose of this study, this was considered sufficient. However, manual correction remains subjective, time-consuming and in the context of Wilms tumours, it is difficult to achieve interobserver agreement [63]. An automated machine learning approach for the segmentation of WTs on multi-parametric MRI might be a useful technique to cope with the interobserver variability. The supplied patient data is crucial in supervised machine learning approaches and as patients with WTs are relatively rare, data is hard to come by [76]. However, the Princes Máxima Center is the current biggest paediatric oncology centre in Europe and this unique position should be used to obtain valuable datasets of paediatric patient with solid tumours. Such an approach may significantly speed up the process and truthfulness of the representation of the oncologic 3D anatomical models.

Thirdly, the clinical impact of 3D anatomical models specifically for WT patients has not yet been prospectively studied in a systematic approach. We suggest to perform a prospective study to compute 3D anatomical models preoperatively for every WT patient. Irtan et al. (2019) describe the use of 3D anatomical models solely for high-risk paediatric surgical oncological procedures and they describe the use of anatomical models in seven renal tumour patients over the course of three years. The models were made on a case-by-case basis, which does not allow a systematic approach. We believe a systematic approach for all patients gives the ability to study the impact more elaborately on the preoperative planning.

Questionnaires for surgeons and urologists can give an insight on how the anatomical models impact surgical decision making. A quantitative evaluation can be performed through comparison of the anatomical models with the pathological specimen to assess the accuracy of the modelling technique. An accuracy evaluation is important to further assess how reliable 3D anatomical models are compared to the patients pathology.

Finally, we advocate the use of a more generalized software package for the segmentation and 3D modelling of paediatric MRIs. One of the main benefits yet also a shortcoming of the developed technique is the specificity of the (semi-)automatic segmentation algorithm. The algorithm is specifically build for the visualisation of the anatomy of WT patients strictly on the MR protocol which these patients currently receive. The modelling of other oncological surgical pathologies requires a whole newly developed algorithm. On the contrary, 3DSlicer is a more general tool for 3D anatomic modelling. The models derived with 3DSlicer were clinically preoperatively used for multiple patients. The 3D models were considered good representative models, except for the vein and UCS models which were considered representative with false information. However, 3DSlicer is not CE-certified and therefore, according to dutch law, not allowed to be used in standard clinical care. Therefore, other options should be evaluated in the near future. In the review of Lupulescu et al. (2019), Mimics Innovation Suite was the most commonly used software package as reported by 6 out of 27 studies [43]. Mimics Innovation Suite by Materialise (Leuven, Belgium) is well-suited for general 3D anatomical modelling and CE-certified. It is a comprehensive medical 3D segmentation software package capable of most standardized segmentation techniques and allows researchers to implement self-written programs through a python interface. In the future, we could implement the proposed MATLAB segmentation algorithm within the interface of Mimics, combining specific and general segmentation software into one user-friendly interface..



# Conclusion

To conclude, we proposed a three dimensional high quality imaging strategy for the visualisation of intraparenchymal arteries and developed a semi-automatic segmentation algorithm for the three dimensional anatomic modelling of Wilms Tumour patients. The b-SSFP sequence is robust and it shows an improved image quality in comparison to the standard contrast-enhanced magnetic resonance angiography and the T2-weighted sequence. It is also considered sufficient to substitute the additional computed tomography angiography. Therefore, it should be added to the clinical MRI kidney tumour protocol for the preoperative MRI assessment of neoadjuvant chemotherapy and preoperative planning.

The segmentation algorithm produced clinically relevant arterial models. Tumour and kidney models were considered of representative quality. The vein and urine collection system models were unrepresentative of the patient specific anatomy. Further development of these segmentation algorithms is necessary and can be improved through more specific imaging techniques.



## Appendix A

# SIOP staging for renal tumours

Table A.1: SIOP staging for renal tumours, derived from Metzger et al. (2005) [5]

Stage	Description
I	(a) Tumour is limited to kidney or surrounded with fibrous pseudocapsule if outside of the normal contours of the kidney, the renal capsule or pseudocapsule may be infiltrated with the tumour, but it does not reach the outer surface, and is completely resected (resection margins "clear") (b) The tumour may be protruding into the pelvic system and "dipping" into the ureter (but it is not infiltrating their walls) (c) The vessels of the renal sinus are not involved (d) Intrarenal vessel involvement may be present
II	(a) The tumour extends beyond kidney or penetrates through the renal capsule and/or fibrous pseudocapsule into perirenal fat but is completely resected (resection margins "clear") (b) The tumour infiltrates the renal sinus and/or invades blood and lymphatic vessels outside the renal parenchyma but is completely resected (c) The tumour infiltrates adjacent organs or vena cava but is completely resected
III	(a) Incomplete excision of the tumour, which extends beyond resection margins (gross or microscopical tumour remains postoperatively) (b) Any abdominal lymph nodes are involved (c) Tumour rupture before or intraoperatively (irrespective of other criteria for staging) (d) The tumour has penetrated through the peritoneal surface (e) tumour thrombi present at resection margins of vessels or ureter, transected or removed piecemeal by surgeon (f) The tumour has been surgically biopsied (wedge biopsy) prior to preoperative chemotherapy or surgery
IV	Hematogenous metastases (lung, liver, bone, brain, etc.) or lymph node metastases outside the abdomino-pelvic region
V	Bilateral renal tumours at diagnosis

## Literature review pediatric NCE-MRA

Matthijs Fitski

Graduate intern, Technical Medicine  
m.fitski-2@prinsesmaximacentrum.nl

**Abstract**— Visualization of the extra- and intraparenchymal vasculature is important for the preoperative assessment of Wilms tumors to judge the eligibility of nephron sparing surgery. The currently used contrast-enhanced magnetic resonance angiogram (CE-MRA) sequence is insufficient, partially due to motion blurring. Therefore, the possibility of a non-contrast-enhanced (NC-) MRA sequence for the visualization of renal arteries of children is reviewed in the literature. The most commonly used NC-MRA sequence in pediatric renal artery assessment is the balanced Steady-State Free-Precession (b-SSFP) sequence. Even though only 4 studies met the search criteria, they do show that b-SSFP is a promising method to visualize all extraparenchymal and possibly intraparenchymal vasculature. Secondly, the use of b-SSFP for the visualization of intraparenchymal arteries in adults was reviewed in the literature. b-SSFP is commonly used in adults for the assessment of Renal artery stenosis (RAS) and evaluation of the vasculature of a living donor for kidney transplantation. 29 studies met the search criteria. Most studies show improved image quality of the intraparenchymal arteries with b-SSFP in comparison to CE-MRA. Based on the current literature, it is concluded that b-SSFP is a promising method for the visualization of extra- and intraparenchymal arteries for the preoperative assessment of Wilms tumors.

### I. INTRODUCTION

Total nephrectomy is the standard surgical procedure for children with an unilateral Wilms tumor. However, these patients have a risk of end-stage renal failure, which is the second most common cause of death in Wilms tumor survivors [1]. If the tumor is smaller than 300ml and if the surgeon expects a substantial amount of functional kidney remnant, nephron sparing surgery (NSS) may be considered. NSS for unilateral disease is controversial as there is a substantial risk positive resection margins, therewith upstaging the tumour and increasing the local recurrence rate. The overall survival after NSS is equal to the overall survival of TN yet surgeons remain hesitant to perform this procedure.

In order to judge whether NSS is feasible, the surgeon assesses the preoperative MRI. Based on the position and size of the tumor and the surrounding vasculature, the surgeon determines the amount of saved functional kidney tissue and expected profit of NSS. The current MRA does not visualize the required vasculature so the surgeon has to judge the vasculature based on the T2 sequence. This sequence does not have an artery / vein distinction making it difficult to judge renal vessels. The current MRA protocol is a 4D contrast-enhanced sequence (CE-MRA). The contrast bolus is injected and when it reaches the aortic arch, the sequence starts rapidly scanning. However, due to respiratory movement of the kidney, the contrast signal is lost in the kidney

Medical supervisor Princess Máxima Center, prof. dr. M.H.W.A. Wijnen  
Technical supervisor University of Twente, dr. F.J.J. Simonis

and only the renal artery/vein are visualized, distinction of the segmental arteries is difficult (vasculature of the kidney is shown in figure 1).

Clear distinction of the extraparenchymal arteries and possibly intraparenchymal arteries is important for the preoperative assessment of children with Wilms tumor to determine their eligibility for NSS. The CE-MRA is conceivably not suited for this application due to the required scanning speed and the lack of motion compensation techniques. Therefore, we are looking for a non-contrast-enhanced MRA (NCE-MRA) sequence which can at least visualize the extraparenchymal arteries and is suitable for children. As there is a large amount of possible NC-MRA sequences, a literature search was performed to determine which sequence is most commonly used for the visualization of renal arteries in children. Secondly, an additional literature search was required to assess how the NC-MRA technique is used and optimized to visualize the extra- and intraparenchymal arteries in adults.

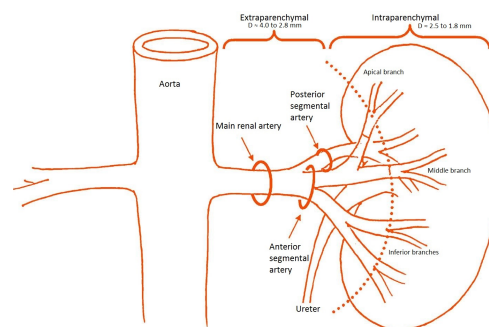


Fig. 1: Schematic overview of the average extraparenchymal and intraparenchymal renal vasculature, courtesy of Klatte et al. 2015 (D = diameter) [2]. A NC-MRA must visualize extraparenchymal arteries and visualization of the intraparenchymal arteries is favorable. Vasculature sizes are derived from Macchi et al. 2017 [3].

### II. CURRENT LITERATURE NCE-MRA IN CHILDREN

#### A. Method

A literature search was performed by M.F. We searched PubMed and EMBASE for studies with the following terms in either the title or the abstract: "pediatric", "MRA", "non-contrast-enhanced", "b-SSFP", "ASL", "QISS", "PC", "TOF", "FSE", "TSE", "FSD" and "renal artery". A complete overview of the different search

terms and their relation are shown in table I. The reference list of the resulting studies were manually assessed to confirm no studies were missed. Abstracts from relevant scientific meetings were also included. Irrelevant studies, e.g. not concerning the renal arteries or children, were manually excluded.

TABLE I: Search criteria for PubMed and EMBASE. All synonyms, spelling in both British and American English, both single and plural and abbreviations were included.

Children	or Pediatric or Paediatric or Infant or Young adult
and MRA	or Magnetic Resonance Angiography or MR Angiography or MR-Angiography
and Non-contrast	or Non-contrast-enhanced or Unenhanced or Non-enhanced or NCE or NC or all NC-MRA-sequences: b-SSFP, ASL, QISS, PC, TOF, FSE, TSE, FSD
and Renal artery	or Kidney or Renal
not Extremities	or Cerebral or Peripheral

### B. Results

In total, 13 studies or abstracts were included with our searching criteria. 1 study was excluded due to a focus on the thoracic aorta instead of the renal artery, 1 study was excluded due to not being related to pediatrics. 2 abstracts were excluded, one did not concern children and one was an educational exhibit. 4 studies and 5 abstracts met all search criteria and were included for the literature review. The manual assessment of the reference lists of the 4 studies resulted in no additional studies.

### C. Discussion

NC-MRA is currently not commonly used to visualize the extra- and intraparenchymal arteries in pediatrics. Klee et al. 2012 describe the use of an ECG-gated, free breathing, balanced steady-state free-precession (b-SSFP) sequence for the visualization of the renal arteries in children [4]. The renal arteries of fourteen boys and seven girls (mean age 9.7 years, range 7 weeks to 17 years) were visualized at 1.5 tesla (T) with b-SSFP. Two experienced radiologists assessed the resulting MRAs on a four-point scale. They concluded that the visualization of the abdominal aorta and renal artery were excellent, the segmental extraparenchymal arteries were good and the intraparenchymal arteries were acceptable (example given in figure 2). There was no difference in image quality between sedated and non-sedated children therewith indicating that there is no need for breath-holding. The NC-MRAs of very young children showed a stair-step artifact at the intraparenchymal arteries.



Fig. 2: Coronal oblique maximum intensity projection resulting from the b-SSFP sequence by Klee et al. 2012 showing excellent image quality up to and including the intraparenchymal arteries [4].

An application of the b-SSFP sequence for pediatric renal vasculature imaging was also described by Serai et al. 2012 [5]. They stress the advantages of b-SSFP such as a higher signal-to-noise ratio, faster acquisition times and an increased flow-insensitivity in comparison to other non-contrast sequences. Their sequence takes roughly 3 min to scan and may reach a resolution of approximately 1 mm. Figure 3 illustrates the results of their proposed technique.



Fig. 3: Anterior posterior maximum intensity projection from the b-SSFP technique as described by Serai et al. 2012 [5]. The dashed arrow marks the mesenteric artery, the regular arrows mark the renal arteries.

NC-MRA was used by two different studies for detecting crossing renal vessels in children and the results were compared with surgical findings [6], [7]. Brucher et al. 2016 used b-SSFP combined with Time-SLIP (section III) to evaluate crossing renal veins in ten girls and nine boys, older than 4 years (age 4 - 16, mean 9 years). It was concluded that 88% of the images had a fair or improved image quality for visualization of the renal arteries. Sertorio et al. 2018 performed the same study, but with 17 boys and 12 girls younger than 4 years (1 month to 4 years old, mean 20 months) [7]. They found a fair or improved image quality in 85% of the patients.

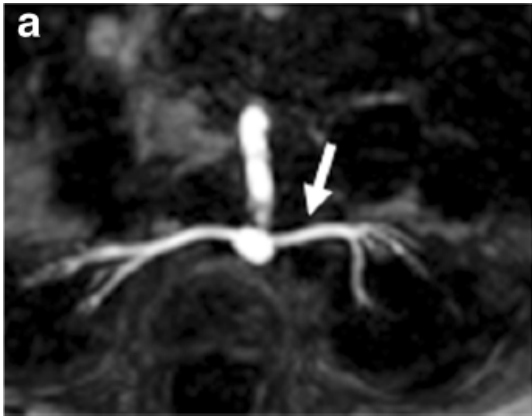


Fig. 4: Axial non-enhanced gradient echo showing both extra- and intraparenchymal arteries in infants, courtesy of Sertorio et al. 2018 [7].

An example is given in figure 4. They also state that the NC-MRA outperformed the CE-MRA in detecting crossing renal veins due to the low contrast dose for children in this age group. It should be noted that both authors do not show any data concerning the image quality of intraparenchymal arteries.

#### D. Pilot studies / posters

7 pilot studies have submitted an abstract to multiple scientific meetings. Mendichovszky et al. 2010 performed a feasibility study to assess b-SSFP for the visualization of the renal arteries in children [8]. The scans of 12 patients (mean age 13 years) scored good or excellent for the visualization of the extraparenchymal arteries. Visualization of the intraparenchymal arteries proved difficult and dependent on the inversion time. Dondaldson et al. 2010 compared b-SSFP with a CE-MRA sequence for the assessment of the renal arteries and they showed there were no significant differences in the measurement of the aortic diameter and a significantly higher SNR for the b-SSFP sequence. They claim NC-MRA is comparable to CE-MRA.

Deng et al. 2014 optimized a b-SSFP sequence to visualize renal arteries in children [9]. Their optimization resulted in scans with a good vessel-background contrast, excellent visualization of the extraparenchymal arteries, minimal respiratory motion blurring and minimal venous contamination. The inter-observer agreement of measurement of the renal arteries in b-SSFP images was quantified by Mendichovszky et al. 2010 [10]. Two radiologists measured three distinct regions of the renal arteries of 12 children showing an excellent inter-observer agreement. Before Brucher et al. and Sertorio et al., a pilot study was performed to assess crossing renal vessels with a NC-MRA sequence [11]. The image quality and vascular contrast of both turbo-spin-echo (FSE) and b-SSFP were evaluated. The conclude both sequences with optimized imaging parameters resulted in high quality MRAs of the extraparenchymal arteries.

### III. BALANCED STEADY-STATE FREE-PRECESSION

No studies on NC-MRA techniques in children other than b-SSFP have been published so far. Therefore, further review and applications in adults are focused on b-SSFP. b-SSFP is a gradient-echo sequence in which the dephasing of the spin caused by the gradient is nulled over an interval of the repetition time (TR). This is the "balanced" state, the magnetization is constant both in the longitudinal and transverse direction as shown in figure 5 [12]. This results is a contrast of the T2/T1-ratio, instead of exclusively T1 or T2 weighing. The T2/T1-ratio is especially high for blood in comparison to solid tissue. Because the gradient is balanced in all three directions, the sequence is intrinsically flow-compensated making it useful for vasculature imaging [13]. The b-SSFP has a different nomenclature for different vendors; TrueFISP by Siemens, b-FFE by Philips or FIESTA by GE. B-SSFP can not differentiate between arteries and veins on itself. Therefore, certain compensation methods can be used to either suppress venous inflow or enhance arterial inflow. Arterial inflow-enhancement is commonly used in renal NC-MRA. A  $180^\circ$  RF saturation pulse is used to saturate all the background signal. Unsaturated blood flows in the saturated volume and after a blood travel time it is imaged with a rapid b-SSFP sequence. This creates a higher T2/T1 ratio between saturated background and unsaturated fresh arterial blood. An optimal blood travel time should allow the fresh blood to replace the inverted saturated blood in the target volume [14]. Inflow-enhancement combined with b-SSFP is called syngo NATIVE TrueFISP by Siemens, b-TRANCE by Philips, Time-SLIP by Toshiba and IFIR by GE. Both regular b-SSFP and inflow-enhanced b-SSFP can be respiratory triggered to reduce motion blurring.

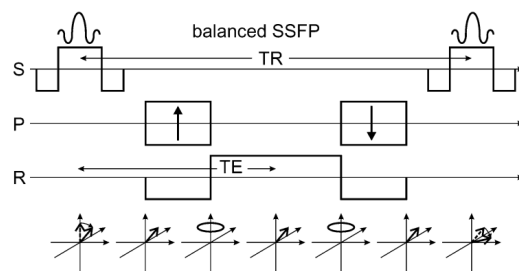


Fig. 5: A schematic overview of the b-SSFP pulse sequence showing a balanced magnetization, both longitudinal and transverse direction, in the lower right figure. The S-axis is the Slice selection, the P-axis is the Phase encoding and the R-axis is the Read gradient. Courtesy of Scheffler et al. 2003 [12].

### IV. CURRENT LITERATURE B-SSFP FOR ADULTS

#### A. Method

A literature search was executed roughly similar as before. However, now all search terms for NC-MRA techniques were removed except for the terms concerning b-SSFP.

Additionally, the children section was searched with NOT instead of AND to exclude pediatric studies. Subsequently, studies concerning children, with no focus on the renal arteries or abstracts were manually excluded.

### B. Results

53 studies were included with our search criteria. 11 studies were excluded because they were a conference abstract, 2 studies were excluded because they were children-related [4], [5]. 10 studies were excluded because there was no focus on the renal arteries. In total, 29 studies met all search criteria and were included after the manual assessment.

### C. Discussion

The b-SSFP sequence is most commonly used and studied clinically for the assessment of renal artery stenosis (RAS) [14]–[26]. Additionally, it is also used to evaluate the vasculature of the live donor for kidney transplantation [27]–[33]. The clinical experience of the b-SSFP sequence has been reported by three studies [34]–[36]. Three studies describe a b-SSFP technique with a breath-hold [36]–[38]. Xie et al. 2015 report the use of a self-gating system instead of a respiratory trigger for b-SSFP [39]. Both Shonai et al. 2008 and Stafford et al. 2009 report a novel b-SSFP sequence for the visualization of proximal renal arteries [40], [41]. Important studies are further discussed.

Glockner et al. 2010 evaluated free-breathing b-SSFP (N=67) for the detection of RAS and compared the sequence with contrast-enhanced MRA (N=64) [25]. The NC-MRA technique showed a sensitivity of 94% (reader 1) and 82% (reader 2) and specificity of 82% and 87% in comparison to the ground truth, the CE-MRA. On a 5-point scale, the overall image quality of CE-MRA were rated  $3.9 \pm 0.7$  and the overall image quality of the NC-MRA was rated  $3.7 \pm 1.0$  indicating acceptable image quality for both modalities with no significant difference. They stress that the FOV of the NC-MRA sequence decreases the diagnostic confidence significantly ( $4.3 \pm 0.8$  for CE-MRA vs  $3.7 \pm 1.0$  for NC-MRA). However, the NC-MRA technique often showed superior visualization of the intraparenchymal arteries. They state that this may be related due to the very rapid transit time of the contrast dose in CE-MRA between renal arteries and veins and opacification of the renal parenchyma. An example of intraparenchymal artery visualization is given in figure 6. In the study of Braidy et al 2012, slightly better sensitivity and specificity were determined (85% and 96%) for the detection of RAS. They again state a slightly superior visualization of the intraparenchymal arteries with b-SSFP (moderate) in comparison to CE-MRA (bad) [17].

The relationship between age, blood velocity, T1 value and image quality was assessed by Kurata et al. 2016 [42]. The optimal T1 for patients below 50 years is 1600 and 1800 ms. 1600 ms resulted in the best Vessel-to-Kidney ratio whereas 1800 ms resulted in superior results during a qualitative assessment by two radiologists. The image quality was scored on a 4-point scale at 1600 ms and 1800 ms. For the second branch of the renal artery, at 1600 ms, the image

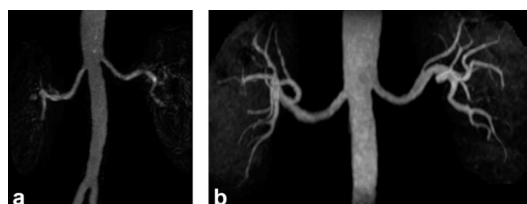


Fig. 6: Anterior posterior maximum intensity projection of a normal contrast enhanced sequence (a) and the b-SSFP sequence. Glockner et al. 2010 show improved visualization of the intraparenchymal arteries in adults with b-SSFP [25].

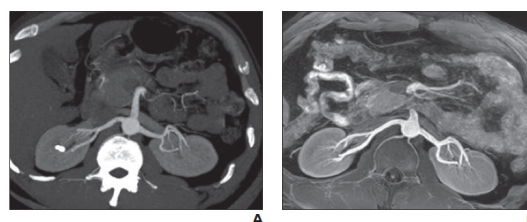


Fig. 7: Comparison of an axial CTA (A) and NC-MRA (B) of a 35 year old male patient. Courtesy of Albert et al. 2003 [16].

quality was  $3.2 \pm 0.75$  and at 1800 ms, the image quality was  $3.2 \pm 0.95$  (both scores are averaged between two readers). This shows they were able to visualize the second renal artery with a good image quality or better (N=42).

75 patients were included in a prospective multicenter study to compare b-SSFP with Time-SLIP to Computed Tomography Angiography (CTA) for the detection of RAS by Albert et al. 2013 [16]. Again, MRA proved to show excellent image quality in the majority of the patients (75%) and only showed poor image quality in 3%. However, CTA showed excellent image quality in 91% of the patients (example show in figure 7). It is concluded that inflow-enhanced b-SSFP is a safe technique for the diagnosis of RAS in adults.

The best tagging location for b-SSFP combined with Time-SLIP has been reported by Zhang et al. 2014 [43]. They scanned 36 volunteers twice with different tagging pulses, one placed just above the superior pole of the kidney and one superior to the origination the renal arteries (figure 8). Scans were evaluated by two expert readers on a 4-point scale. The image quality of the intraparenchymal arteries was  $3.03 \pm 0.65$  at the superior pole tagging position. The image quality of the intraparenchymal arteries was  $3.2 \pm 0.72$  at the renal artery tagging position.

[36]

### V. CONCLUSION

The most commonly used non-contrast MRA technique for the visualization of the renal arteries in children is the b-SSFP sequence. However, literature is scarce. Many pilot studies do show that b-SSFP should be able to visualize

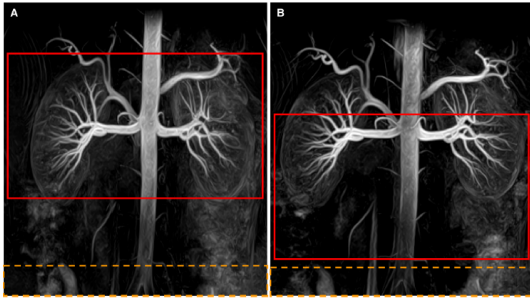


Fig. 8: Two anterior posterior maximum intensity projections scanned with b-SSFP with Time-SLIP sequences at different tagging locations in the same volunteer by Zhang et al. 2014: at the superior pole of the kidney (A) and superior to the origination of the renal arteries (B) as depicted with the red frame. The dashed orange frame is the used saturation band. [43].

intraparenchymal arteries in children. B-SSFP is commonly used in adults for the diagnosis of renal artery stenosis and for the assessment of the vasculature of a living kidney donor. In adults, good visualization of the intraparenchymal arteries is already feasible.

#### REFERENCES

- [1] C. A. Cotton, S. Peterson, P. A. Norkool, J. Takashima, Y. Grigoriev, and N. E. Breslow, "Early and late mortality after diagnosis of wilms tumor," *Journal of Clinical Oncology*, vol. 27, no. 8, p. 1304, 2009.
- [2] T. Klatte, V. Ficarra, C. Gratzke, J. Kaouk, A. Kutikov, V. Macchi, A. Mottrie, F. Porpiglia, J. Porter, C. G. Rogers et al., "A literature review of renal surgical anatomy and surgical strategies for partial nephrectomy," *European urology*, vol. 68, no. 6, pp. 980–992, 2015.
- [3] V. Macchi, A. Crestani, A. Porzionato, M. M. Sfriso, A. Morra, M. Rossanese, G. Novara, R. De Caro, and V. Ficarra, "Anatomical study of renal arterial vasculature and its potential impact on partial nephrectomy," *BJU international*, vol. 120, no. 1, pp. 83–91, 2017.
- [4] D. Klee, R. S. Lanzman, D. Blondin, P. Schmitt, J. Oh, B. Salgin, E. Mayatepek, G. Antoch, and J. Schaper, "Non-enhanced eeg-gated respiratory-triggered 3-d steady-state free-precession mr angiography with slab-selective inversion: Initial experience in visualisation of renal arteries in free-breathing children without renal artery abnormality," *Pediatric Radiology*, vol. 42, no. 7, pp. 785–790, 151939720 2012-04-03 2012-08-15.
- [5] S. Serai, A. J. Towbin, and D. J. Podberesky, "Non-contrast mra using an inflow-enhanced, inversion recovery ssfp technique in pediatric abdominal imaging," *Pediatric Radiology*, vol. 42, no. 3, pp. 364–368, 151709404 2011-11-11 2012-07-17.
- [6] N. Brucher, J. Vial, C. Baunin, D. Labarre, O. Meyrignac, M. Juricic, O. Bouali, O. Abbo, P. Galinier, and N. Sans, "Non-contrast-enhanced mr angiography using time-spin labelling inversion pulse technique for detecting crossing renal vessels in children with symptomatic ureteropelvic junction obstruction: comparison with surgical findings," *European Radiology*, vol. 26, no. 8, pp. 2697–2704, 1606696225 2015-11-06 2016-07-20.
- [7] F. Sertorio, M. C. Y. Wong, V. Incarboni, A. Pistorio, G. Mattioli, G. M. Magnano, and M. B. Damasio, "Non-contrast-enhanced magnetic resonance angiography for detecting crossing renal vessels in infants and young children: comparison with contrast-enhanced angiography and surgical findings," *Pediatric radiology*, pp. 1–9, 2018.
- [8] I. Mendichovszky, S. Donaldson, K. Hindle, A. Jackson, and A. Shabani, "Non-contrast-enhanced mr angiography of renal arteries in pediatric patients: A feasibility study," *Pediatric Radiology*, vol. 40, no. 6, pp. 1080–1081, 170423664 2011-05-31.
- [9] J. Deng, C. Rigsby, M. Messina, S. Bero, and G. McNeal, "Optimization of native truefisp protocol for non-contrast renal mra," *Pediatric Radiology*, vol. 44, pp. S212–S213, 171589113 2014-08-23.
- [10] I. Mendichovszky, A. Jackson, and A. Shabani, "Inter-observer reproducibility of non contrast-enhanced mr angiography of renal arteries in pediatric patients," *Pediatric Radiology*, vol. 40, no. 6, p. 1122, 170423797 2011-05-31.
- [11] J. Carmichael and C. Lloyd, "Optimization of non-contrast mr angiography for the assessment of crossing renal vessels in children with pelvi-ureteric junction obstruction," *Pediatric Radiology*, vol. 43, p. S551, 171121511 2013-07-29.
- [12] K. Scheffler and S. Lehnhardt, "Principles and applications of balanced ssfp techniques," *European radiology*, vol. 13, no. 11, pp. 2409–2418, 2003.
- [13] G. B. Chavhan, P. S. Babyn, B. G. Jankharia, H.-L. M. Cheng, and M. M. Shroff, "Steady-state mr imaging sequences: physics, classification, and clinical applications," *Radiographics*, vol. 28, no. 4, pp. 1147–1160, 2008.
- [14] I. Parienty, G. Rostoker, F. Jouniaux, M. Piotin, F. Admiraal-Behloul, and M. Miyazaki, "Renal artery stenosis evaluation in chronic kidney disease patients : Nonenhanced time-spatial labeling inversion-pulse three-dimensional mr angiography with regulated breathing versus dsa," *Radiology*, vol. 259, no. 2, pp. 592–601, 1361634674 2011-04-28 2011-05-04.
- [15] M. G. Angeretti, D. Lumia, A. Cani, M. Barresi, L. Nocchi Cardim, F. Piacentino, A. M. Maresca, R. Novario, E. A. Genovese, and C. Fugazzola, "Non-enhanced mr angiography of renal arteries: comparison with contrast-enhanced mr angiography," *Acta radiologica (Stockholm, Sweden : 1987)*, vol. 54, no. 7, pp. 749–756, 1370142410 2013-11-05.
- [16] T. E. Albert, M. Akahane, I. Parienty, N. Yellin, V. Catalá, X. Alomar, A. Prot, N. Tomizawa, H. Xue, V. S. Katabathina, J. E. Lopera, and Z. Jin, "An international multicenter comparison of time-slip unenhanced mr angiography and contrast-enhanced ct angiography for assessing renal artery stenosis: The renal artery contrast-free trial," *American Journal of Roentgenology*, vol. 204, no. 1, pp. 182–188, 1604054436 2015-05-05 2015-05-07.
- [17] C. Braidy, I. Daou, A. D. Diop, O. Helweh, C. Gageanu, L. Boyer, and P. Chabrot, "Unenhanced mr angiography of renal arteries: 51 patients," *American Journal of Roentgenology*, vol. 199, no. 5, pp. W629–W637, 1365936222 2012-11-06 2012-11-14.
- [18] T. A. Bley, C. J. François, M. L. Schiebler, O. Wieben, N. Takei, J. H. Brittain, A. M. Del Rio, T. M. Grist, and S. B. Reeder, "Non-contrast-enhanced mra of renal artery stenosis: validation against dsa in a porcine model," *European Radiology*, vol. 26, no. 2, pp. 547–555, 1604623803 2015-06-05 2016-01-26.
- [19] M. Iida, H. Maeda, M. Yamamoto, M. Yamazaki, H. Honjo, I. Kodama, and K. Kamiya, "Association of renal artery stenosis with aortic jet velocity in hypertensive patients with aortic valve sclerosis," *American Journal of Hypertension*, vol. 23, no. 2, pp. 197–201, 150718029 2010-02-10 2010-02-23.
- [20] M. M. Y. Khoo, D. Deeab, W. M. W. Gedroyc, N. Duncan, D. Taube, and E. A. Dick, "Renal artery stenosis: Comparative assessment by unenhanced renal artery mra versus contrast-enhanced mra," *European Radiology*, vol. 21, no. 7, pp. 1470–1476, 151286806 2011-02-22 2011-07-04.
- [21] C. Sebastià, A. D. Sotomayor, B. Paño, R. Salvador, M. Burrel, A. Botey, and C. Nicolau, "Accuracy of unenhanced magnetic resonance angiography for the assessment of renal artery stenosis," *European Journal of Radiology Open*, vol. 3, pp. 200–206, 1611525656 2016-08-09 2016-08-12.
- [22] W. J. Tao, Y. Shen, L. L. Guo, and G. J. Bo, "Role of non-contrast balanced steady-state free precession magnetic resonance angiography compared to contrast-enhanced magnetic resonance angiography in diagnosing renal artery stenosis: A meta-analysis," *Chinese Medical Journal*, vol. 127, no. 19, pp. 3483–3490, 1600097582 2014-10-11 2014-11-10.
- [23] W. Zhang, Y. Qian, J. Lin, P. Lv, K. Karunanithi, and M. Zeng, "Hemodynamic analysis of renal artery stenosis using computational fluid dynamics technology based on unenhanced steady-state free precession magnetic resonance angiography: Preliminary results," *International Journal of Cardiovascular Imaging*, vol. 30, no. 2, pp. 367–375, 152905713 2013-12-11 2014-05-07.
- [24] G. J. Wilson and J. H. Maki, "Non-contrast-enhanced mr imaging of

- renal artery stenosis at 1.5 tesla," *Magnetic Resonance Imaging Clinics of North America*, vol. 17, no. 1, pp. 13–27, 1354440242 2009-04-30.
- [25] J. F. Glockner, N. Takahashi, A. Kawashima, D. A. Woodrum, D. W. Stanley, N. Takei, M. Miyoshi, and W. Sun, "Non-contrast renal artery mra using an inflow inversion recovery steady state free precession technique (inhance): Comparison with 3d contrast-enhanced mra," *Journal of Magnetic Resonance Imaging*, vol. 31, no. 6, pp. 1411–1418, 1358895165 2010-06-04 2010-06-25.
- [26] O. K. Mohrs, S. E. Petersen, T. Schulze, M. Zieschang, H. Kux, P. Schmitt, S. Bergemann, and H. U. Kauczor, "High-resolution 3d unenhanced ecg-gated respiratory-navigated mr angiography of the renal arteries: Comparison with contrast-enhanced mr angiography," *American Journal of Roentgenology*, vol. 195, no. 6, pp. 1423–1428, 1360086562 2010-12-14 2010-12-20.
- [27] R. Goetti, S. Baummueller, H. Alkadhi, P. A. Clavien, M. Schiesser, T. Pfammatter, R. Hunziker, and G. Puippe, "Diagnostic performance of a non-contrast-enhanced magnetic resonance imaging protocol for potential living related kidney donors," *Academic Radiology*, vol. 20, no. 4, pp. 393–400, 1368540545 2013-03-25 2013-03-29.
- [28] I. Laurence, B. Ariff, R. A. Quest, S. Moser, A. Glover, D. Taube, P. Gishen, V. Papalois, and C. Juli, "Is there a role for free breathing non-contrast steady-state free precession renal mra imaging for assessing live donors? a preliminary study," *British Journal of Radiology*, vol. 85, no. 1016, pp. e448–e454, 1365407858 2012-08-17 2012-08-27.
- [29] A. Patil, K. Shailage, J. Nadarajah, P. Harigovind, and R. Mohan, "Comparison of computed tomographic angiography and noncontrast magnetic resonance angiography in preoperative evaluation of living renal donors," *Indian Journal of Urology*, vol. 33, no. 1, pp. 30–35, 1614049302 2017-01-17.
- [30] A. D. Blankholm, B. Ginneer-Pedersen, B. Stausbøl-Grøn, M. Haislund, S. Laustsen, and S. Ringgaard, "Non-contrast enhanced magnetic resonance angiography techniques in candidates for kidney transplantation: A comparative study," *Radiography*, vol. 19, no. 3, pp. 212–217, 152565826 2013-05-08 2013-08-07.
- [31] R. S. Lanzman, A. Voiculescu, C. Walther, A. Ringelstein, X. Bi, P. Schmitt, S. M. Freitag, S. Won, A. Scherer, and D. Blondin, "Ec-gated nonenhanced 3d steady-state free precession mr angiography in assessment of transplant renal arteries: Comparison with dsa," *Radiology*, vol. 252, no. 3, pp. 914–921, 1355299949 2009-11-04.
- [32] E. M. Bultman, J. Klaers, K. M. Johnson, C. J. François, M. L. Schiebler, S. B. Reeder, and W. F. Block, "Non-contrast enhanced 3d ssfp mra of the renal allograft vasculature: A comparison between radial linear combination and cartesian inflow-weighted acquisitions," *Magnetic Resonance Imaging*, vol. 32, no. 2, pp. 190–195, 152869655 2013-11-21 2014-01-24.
- [33] X. Liu, N. Berg, J. Sheehan, X. Bi, P. Weale, R. Jerecic, and J. Carr, "Renal transplant: Nonenhanced renal mr angiography with magnetization-prepared steady-state free precession," *Radiology*, vol. 251, no. 2, pp. 535–542, 1354650703 2009-06-24.
- [34] I. P. Atanasova, R. P. Lim, H. Chandarana, P. Storey, M. T. Bruno, D. Kim, and V. S. Lee, "Quadruple inversion-recovery b-ssfp mra of the abdomen: Initial clinical validation," *European Journal of Radiology*, vol. 83, no. 9, pp. 1612–1619, 153224337 2014-07-09 2014-09-06.
- [35] X. Chen, C. C. Xia, J. Y. Sun, C. X. Li, Y. Yuan, H. H. Tang, B. Song, and Z. L. Li, "Nonenhanced renal artery mr angiography with time spatial labeling inversion pulse technology and its clinical values," *Sichuan Da Xue Xue Bao Yi Xue Ban*, vol. 41, no. 5, pp. 881–4, 2010, chen, Xian Xia, Chun-chao Sun, Jia-yu Li, Chang-xian Yuan, Yuan Tang, He-han Song, Bin Li, Zhen-lin English Abstract Evaluation Studies Journal Article China Sichuan Da Xue Xue Bao Yi Xue Ban. 2010 Sep;41(5):881-4.
- [36] P. W. Worters, M. Saranathan, A. Xu, and S. S. Vasanawala, "Inversion-recovery-prepared dixon bssfp: Initial clinical experience with a novel pulse sequence for renal mra within a breathhold," *Journal of Magnetic Resonance Imaging*, vol. 35, no. 4, pp. 875–881, 1364483944 2012-03-29 2012-04-02.
- [37] M. Saranathan, E. Bayram, P. W. Worters, and J. F. Glockner, "A 3d balanced-ssfp dixon technique with group-encoded k-space segmentation for breath-held non-contrast-enhanced mr angiography," *Magnetic Resonance Imaging*, vol. 30, no. 2, pp. 158–164, 151696893 2011-11-04 2012-01-18.
- [38] H. Tan, I. Koktzoglou, C. Glielmi, M. Galizia, and R. R. Edelman, "Optimization of single shot 3d breath-hold non-enhanced mr angiography of the renal arteries," *Journal of Cardiovascular Magnetic Resonance*, vol. 14, no. 1, 152097483 2012-07-09 2012-09-04.
- [39] Y. Xie, Z. Fan, R. Saouaf, Y. Natsuaki, G. Laub, and D. Li, "Adaptive online self-gating (adios) for free-breathing noncontrast renal mr angiography," *Magnetic Resonance in Medicine*, vol. 73, no. 1, pp. 312–317, 152988845 2014-02-05 2015-01-13.
- [40] T. Shonai, T. Takahashi, H. Ikeguchi, M. Miyazaki, K. Amano, and M. Yui, "Improved arterial visibility using short-tau inversion-recovery (stir) fat suppression in non-contrast-enhanced time-spatial labeling inversion pulse (time-slip) renal mr angiography (mra)," *Journal of Magnetic Resonance Imaging*, vol. 29, no. 6, pp. 1471–1477, 1354702551 2009-06-25.
- [41] R. B. Stafford, M. Sabati, M. J. Haakstad, H. Mahallati, and R. Frayne, "Unenhanced mr angiography of the renal arteries with balanced steady-state free precession dixon method," *AJR Am J Roentgenol*, vol. 191, no. 1, pp. 243–6, 2008, 1546-3141 Stafford, Randall B Sabati, Mohammad Haakstad, Michael J Mahallati, Houman Frayne, Richard Journal Article Research Support, Non-U.S. Gov't United States AJR Am J Roentgenol. 2008 Jul;191(1):243-6. doi: 10.2214/AJR.07.3076.
- [42] Y. Kurata, A. Kido, K. Fujimoto, K. Kiguchi, K. Takakura, Y. Moribata, F. Shitano, Y. Himoto, Y. Fushimi, T. Okada, and K. Togashi, "Optimization of non-contrast-enhanced mr angiography of the renal artery with three-dimensional balanced steady-state free-precession and time-spatial labeling inversion pulse (time-slip) at 3t mri, in relation to age and blood velocity," *Abdom Radiol (NY)*, vol. 41, no. 1, pp. 119–26, 2366-0058 Kurata, Yasuhisa Kido, Aki Fujimoto, Koji Kiguchi, Kayo Takakura, Kyoko Moribata, Yusaku Shitano, Fuki Himoto, Yuki Fushimi, Yasutaka Okada, Tomohisa Togashi, Kaori Journal Article Research Support, Non-U.S. Gov't United States Abdom Radiol (NY). 2016 Jan;41(1):119-26. doi: 10.1007/s00261-015-0608-4.
- [43] Y. Zhang, Z. Xing, Y. Liu, D. She, Z. Zeng, and D. Cao, "Nonenhanced renal mr angiography using steady-state free precession (ssfp) and time-spatial labeling inversion pulse (time-slip): repeatability and comparison of different tagging location," *Abdominal Imaging*, 153082632 2014-04-04.

# Rigid alignment

The multiple sequences have to be spatially aligned to ensure they are all in the same coordinate system. This way, the 3D segmentation results match in location and relative size when combined during the visualisation. The rigid alignment algorithm uses the `GetTransformMatrix` function to determine a transform matrix, based on the work of Yaman [77]. The transformation matrix determines how the "moving" MRI sequence is moved to match with the "fixed" MRI sequence to align them in the same coordinate system. Four DICOM parameters are used: `ImagePositionPatient` (IPP), `ImageOrientationPatient` (IOP), `PixelSpacing` (PS) and `SpacingBetweenSlices` (SBS).  $T$  is equal to the translation matrix derived from IPP,  $R$  represents the rotation matrix derived from IOP and  $S$  is equal to the scaling matrix derived from the PS and SBS. These four DICOM parameters are always available in medical imaging data. All matrices are 4 x 4. The function is given in equation 6:

$$M_{Moving} = T_{IPP} * R_{IOP} * S_{SBS} * T_0 \quad (6)$$

$$M_{Fixed} = T_{IPP} * R_{IOP} * S_{SBS} * T_0 \quad (7)$$

$$M_{Alignment} = \frac{M_{Moving}}{M_{Fixed}} \quad (8)$$

Subsequently, the MATLAB function `imwarp` matches the "moving" with the "fixed" with the image size of the "fixed" image according to the 4 x 4 transformation matrix  $M_{Alignment}$  resulting from equation 8. The resulting "moving" image has the same position, orientation and matrix size as the "fixed" image.  $M_{Alignment}$  can also be used to transform the 3D anatomical model instead of the sequence.

# Bibliography

- [1] T. Klatte, V. Ficarra, C. Gratzke, J. Kaouk, A. Kutikov, V. Macchi, A. Mottrie, F. Porpiglia, J. Porter, C. G. Rogers *et al.*, “A literature review of renal surgical anatomy and surgical strategies for partial nephrectomy,” *European urology*, vol. 68, no. 6, pp. 980–992, 2015.
- [2] F. Sertorio, M. C. Y. Wong, V. Incarbone, A. Pistorio, G. Mattioli, G. M. Magnano, and M. B. Damasio, “Non-contrast-enhanced magnetic resonance angiography for detecting crossing renal vessels in infants and young children: comparison with contrast-enhanced angiography and surgical findings,” *Pediatric Radiology*, pp. 1–9, 2018.
- [3] D. W. McRobbie, E. A. Moore, M. J. Graves, and M. R. Prince, *MRI from Picture to Proton*. Cambridge university press, 2017.
- [4] H. Tan, I. Koktzoglou, C. Glielmi, M. Galizia, and R. R. Edelman, “Optimization of single shot 3d breath-hold non-enhanced mr angiography of the renal arteries,” *Journal of Cardiovascular Magnetic Resonance*, vol. 14, no. 1, p. 30, 2012.
- [5] M. L. Metzger and J. S. Dome, “Current therapy for wilms tumor,” *The oncologist*, vol. 10, no. 10, pp. 815–826, 2005.
- [6] G. Pastore, A. Znaor, F. Spreafico, N. Graf, K. Pritchard-Jones, and E. Steliarova-Foucher, “Malignant renal tumours incidence and survival in european children (1978–1997): report from the automated childhood cancer information system project,” *European journal of cancer*, vol. 42, no. 13, pp. 2103–2114, 2006.
- [7] N. E. Breslow, J. M. Lange, D. L. Friedman, D. M. Green, M. M. Hawkins, M. F. Murphy, J. P. Neglia, J. H. Olsen, S. M. Peterson, C. A. Stiller *et al.*, “Secondary malignant neoplasms after wilms tumor: an international collaborative study,” *International journal of cancer*, vol. 127, no. 3, pp. 657–666, 2010.
- [8] D. Green, “Wilms’ tumour,” *European Journal of Cancer*, vol. 33, no. 3, pp. 409–418, 1997.
- [9] M. Malogolowkin, F. Spreafico, J. S. Dome, H. van Tinteren, K. Pritchard-Jones, M. van den Heuvel-Eibrink, C. Bergeron, J. de Kraker, N. Graf, C. R. T.

- Committee, and the SIOP Renal Tumor Study Group, "Incidence and outcomes of patients with late recurrence of wilms' tumor," *Pediatric blood & cancer*, vol. 60, no. 10, pp. 1612–1615, 2013.
- [10] H. L. Neville and M. L. Ritchey, "Wilms' tumor: Overview of national wilms' tumor study group results," *Urologic Clinics of North America*, vol. 27, no. 3, pp. 435–442, 2000.
- [11] S. Dumoucel, M. Gauthier-Villars, D. Stoppa-Lyonnet, P. Parisot, H. Brisse, P. Philippe-Chomette, S. Sarnacki, L. Boccon-Gibod, S. Rossignol, C. Baumann *et al.*, "Malformations, genetic abnormalities, and wilms tumor," *Pediatric blood & cancer*, vol. 61, no. 1, pp. 140–144, 2014.
- [12] N. Graf, H. van Tinteren, C. Bergeron, F. Pein, M. M. van den Heuvel-Eibrink, B. Sandstedt, J.-P. Schenk, J. Godzinski, F. Oldenburger, R. Furtwängler *et al.*, "Characteristics and outcome of stage ii and iii non-anaplastic wilms tumour treated according to the siop trial and study 93-01," *European Journal of Cancer*, vol. 48, no. 17, pp. 3240–3248, 2012.
- [13] M. M. Van Den Heuvel-Eibrink, J. A. Hol, K. Pritchard-Jones, H. Van Tinteren, R. Furtwängler, A. C. Verschuur, G. M. Vujanic, I. Leuschner, J. Brok, C. Rübe *et al.*, "Position paper: Rationale for the treatment of wilms tumour in the umbrella siop–rtsg 2016 protocol," *Nature Reviews Urology*, vol. 14, no. 12, p. 743, 2017.
- [14] A. Verschuur, H. V. Tinteren, N. Graf, C. Bergeron, B. Sandstedt, and J. de Kraker, "Treatment of pulmonary metastases in children with stage iv nephroblastoma with risk-based use of pulmonary radiotherapy," *Journal of Clinical Oncology*, vol. 30, no. 28, pp. 3533–3539, 2012.
- [15] F. Cozzi, A. Schiavetti, F. Morini, A. Zani, M. Gambino, C. Donfrancesco, and D. A. Cozzi, "Renal function adaptation in children with unilateral renal tumors treated with nephron sparing surgery or nephrectomy," *The Journal of urology*, vol. 174, no. 4 Part 1, pp. 1404–1408, 2005.
- [16] D. C. Miller, M. Schonlau, M. S. Litwin, J. Lai, and C. S. Saigal, "Renal and cardiovascular morbidity after partial or radical nephrectomy," *Cancer: Interdisciplinary International Journal of the American Cancer Society*, vol. 112, no. 3, pp. 511–520, 2008.
- [17] C. A. Cotton, S. Peterson, P. A. Norkool, J. Takashima, Y. Grigoriev, and N. E. Breslow, "Early and late mortality after diagnosis of wilms tumor," *Journal of Clinical Oncology*, vol. 27, no. 8, p. 1304, 2009.

- [18] C. G. Moorman-Voestermans, D. C. Aronson, C. R. Staalman, J. F. Delemarre, and J. de Kraker, "Is partial nephrectomy appropriate treatment for unilateral wilms' tumor?" *Journal of pediatric surgery*, vol. 33, no. 2, pp. 165–170, 1998.
- [19] R. C. Shamberger, K. A. Guthrie, M. L. Ritchey, G. M. Haase, J. Takashima, J. B. Beckwith, G. J. D'angio, D. M. Green, and N. E. Breslow, "Surgery-related factors and local recurrence of wilms tumor in national wilms tumor study 4." *Annals of surgery*, vol. 229, no. 2, p. 292, 1999.
- [20] J. C. Wilde, D. C. Aronson, B. Sznajder, H. Van Tinteren, M. Powis, B. Okoye, G. Cecchetto, G. Audry, J. Fuchs, D. V. Schweinitz *et al.*, "Nephron sparing surgery (nss) for unilateral wilms tumor (uwt): the siop 2001 experience," *Pediatric blood & cancer*, vol. 61, no. 12, pp. 2175–2179, 2014.
- [21] N. G. Cost, J. D. Lubahn, C. F. Granberg, A. I. Sagalowsky, J. E. Wickiser, P. C. Gargollo, L. A. Baker, V. Margulis, and D. Rakheja, "Pathological review of wilms tumor nephrectomy specimens and potential implications for nephron sparing surgery in wilms tumor," *The Journal of urology*, vol. 188, no. 4, pp. 1506–1510, 2012.
- [22] M. K. Richards, A. B. Goldin, P. F. Ehrlich, E. A. Beierle, J. J. Doski, M. Goldfarb, M. Langer, J. G. Nuchtern, S. Vasudevan, and K. W. Gow, "Partial nephrectomy for nephroblastoma: a national cancer data base review," *The American Surgeon*, vol. 84, no. 3, pp. 338–343, 2018.
- [23] K. Kieran, M. A. Williams, J. S. Dome, L. M. McGregor, M. J. Krasin, and A. M. Davidoff, "Margin status and tumor recurrence after nephron-sparing surgery for bilateral wilms tumor," *Journal of pediatric surgery*, vol. 48, no. 7, pp. 1481–1485, 2013.
- [24] S. Irtan, P. F. Ehrlich, and K. Pritchard-Jones, "Wilms tumor: State-of-the-art update, 2016," in *Seminars in pediatric surgery*, vol. 25, no. 5. Elsevier, 2016, pp. 250–256.
- [25] M. Harel, J. H. Makari, and F. A. Ferrer, "Oncology: the role of partial nephrectomy in wilms tumor," *Current urology reports*, vol. 14, no. 4, pp. 350–358, 2013.
- [26] R. I. Lopes and A. Lorenzo, "Recent advances in the management of wilms' tumor," *F1000Research*, vol. 6, 2017.
- [27] C. Mrad, A. Coulomb-Lhermine, M. Tabone, T. Ulinski, G. Audry, and S. Irtan, "Oncologic and nephrologic prognosis impact of the nephron sparing surgery formula for wilms tumours in the umbrella protocol: A single-center experience,"

in *SIOP*, 2019, abstract, unpublished.

- [28] J. D. Mathews, A. V. Forsythe, Z. Brady, M. W. Butler, S. K. Goergen, G. B. Byrnes, G. G. Giles, A. B. Wallace, P. R. Anderson, T. A. Guiver *et al.*, “Cancer risk in 680 000 people exposed to computed tomography scans in childhood or adolescence: data linkage study of 11 million australians,” *Bmj*, vol. 346, p. f2360, 2013.
- [29] G. B. Chavhan, P. S. Babyn, P. John, S.-J. Yoo, and C. K. Rigsby, “Pediatric body mr angiography: principles, techniques, and current status in body imaging,” *American Journal of Roentgenology*, vol. 205, no. 1, pp. 173–184, 2015.
- [30] P. Marckmann, L. Skov, K. Rossen, A. Dupont, M. B. Damholt, J. G. Heaf, and H. S. Thomsen, “Nephrogenic systemic fibrosis: suspected causative role of gadodiamide used for contrast-enhanced magnetic resonance imaging,” *Journal of the American Society of Nephrology*, vol. 17, no. 9, pp. 2359–2362, 2006.
- [31] T. Grobner, “Gadolinium—a specific trigger for the development of nephrogenic fibrosing dermopathy and nephrogenic systemic fibrosis?” *Nephrology Dialysis Transplantation*, vol. 21, no. 4, pp. 1104–1108, 2006.
- [32] B. P. Soares, M. H. Lequin, and T. A. Huisman, “Safety of contrast material use in children,” *Magnetic Resonance Imaging Clinics*, vol. 25, no. 4, pp. 779–785, 2017.
- [33] D. Klee, R. S. Lanzman, D. Blondin, P. Schmitt, J. Oh, B. Salgin, E. Mayatepek, G. Antoch, and J. Schaper, “Non-enhanced ecg-gated respiratory-triggered 3-d steady-state free-precession mr angiography with slab-selective inversion: initial experience in visualisation of renal arteries in free-breathing children without renal artery abnormality,” *Pediatric radiology*, vol. 42, no. 7, pp. 785–790, 2012.
- [34] S. Serai, A. J. Towbin, and D. J. Podberesky, “Non-contrast mra using an inflow-enhanced, inversion recovery ssfp technique in pediatric abdominal imaging,” *Pediatric radiology*, vol. 42, no. 3, pp. 364–368, 2012.
- [35] N. Brucher, J. Vial, C. Baunin, D. Labarre, O. Meyrignac, M. Juricic, O. Bouali, O. Abbo, P. Galinier, and N. Sans, “Non-contrast-enhanced mr angiography using time-spin labelling inversion pulse technique for detecting crossing renal vessels in children with symptomatic ureteropelvic junction obstruction: comparison with surgical findings,” *European radiology*, vol. 26, no. 8, pp. 2697–2704, 2016.

- [36] H. Ahmadi and J.-J. Liu, "3-d imaging and simulation for nephron sparing surgical training," *Current urology reports*, vol. 17, no. 8, p. 58, 2016.
- [37] P. V. Glybochko, L. M. Rapoport, Y. G. Alyaev, E. S. Sirota, E. A. Bezrukov, D. N. Fiev, I. S. Byadretdinov, M. D. Bukatov, A. V. Letunovskiy, and D. O. Korolev, "Multiple application of three-dimensional soft kidney models with localized kidney cancer: A pilot study," *Urologia Journal*, p. 0391560317749405, 2018.
- [38] J. L. Silberstein, M. M. Maddox, P. Dorsey, A. Feibus, R. Thomas, and B. R. Lee, "Physical models of renal malignancies using standard cross-sectional imaging and 3-dimensional printers: a pilot study," *Urology*, vol. 84, no. 2, pp. 268–273, 2014.
- [39] F.-C. von Rundstedt, J. M. Scovell, S. Agrawal, J. Zaneveld, and R. E. Link, "Utility of patient-specific silicone renal models for planning and rehearsal of complex tumour resections prior to robot-assisted laparoscopic partial nephrectomy," *Bju international*, vol. 119, no. 4, pp. 598–604, 2017.
- [40] N. Wake, M. A. Bjurlin, P. Rostami, H. Chandarana, and W. C. Huang, "Three-dimensional printing and augmented reality: Enhanced precision for robotic assisted partial nephrectomy," *Urology*, vol. 116, pp. 227–228, 2018.
- [41] M. E. Westerman, J. M. Matsumoto, J. M. Morris, and B. C. Leibovich, "Three-dimensional printing for renal cancer and surgical planning," *European urology focus*, vol. 2, no. 6, pp. 574–576, 2016.
- [42] F. Porpiglia, R. Bertolo, E. Checcucci, D. Amparore, R. Autorino, P. Dasgupta, P. Wiklund, A. Tewari, E. Liatsikos, C. Fiori *et al.*, "Development and validation of 3d printed virtual models for robot-assisted radical prostatectomy and partial nephrectomy: urologists and patients perception," *World journal of urology*, vol. 36, no. 2, pp. 201–207, 2018.
- [43] C. Lupulescu and Z. Sun, "A systematic review of the clinical value and applications of three-dimensional printing in renal surgery," *Journal of Clinical Medicine*, vol. 8, no. 7, 2019. [Online]. Available: <https://www.mdpi.com/2077-0383/8/7/990>
- [44] J. Fuchs, S. W. Warmann, P. Szavay, H. J. Kirschner, J. F. Schäfer, A. Hennemuth, H. G. Scheel-Walter, H. Bourquain, and H. O. Peitgen, "Three-dimensional visualization and virtual simulation of resections in pediatric solid tumors," *Journal of pediatric surgery*, vol. 40, no. 2, pp. 364–370, 2005.
- [45] J. Fuchs, P. Szavay, G. Seitz, R. Handgretinger, J. Schäfer, and S. Warmann, "Nephron sparing surgery for synchronous bilateral nephroblastoma involving

- the renal hilus,” *The Journal of urology*, vol. 186, no. 4, pp. 1430–1436, 2011.
- [46] O. Girón-Vallejo, D. García-Calderón, R. Ruiz-Pruneda, R. Cabello-Laureano, E. Doménech-Abellán, J. L. Fuster-Soler, and J. I. Ruiz-Jiménez, “Three-dimensional printed model of bilateral wilms tumor: A useful tool for planning nephron sparing surgery,” *Pediatric blood & cancer*, vol. 65, no. 4, p. e26894, 2018.
- [47] L. M. Wellens, J. Meulstee, C. P. van de Ven, C. T. van Scheltinga, A. S. Littooi, M. M. van den Heuvel-Eibrink, M. Fiocco, A. C. Rios, T. Maal, and M. H. Wijnen, “Comparison of 3-dimensional and augmented reality kidney models with conventional imaging data in the preoperative assessment of children with wilms tumors,” *JAMA network open*, vol. 2, no. 4, pp. e192633–e192633, 2019.
- [48] A. Fedorov, R. Beichel, J. Kalpathy-Cramer, J. Finet, J.-C. Fillion-Robin, S. Pujol, C. Bauer, D. Jennings, F. Fennessy, M. Sonka *et al.*, “3d slicer as an image computing platform for the quantitative imaging network,” *Magnetic resonance imaging*, vol. 30, no. 9, pp. 1323–1341, 2012.
- [49] N. Schieda, I. Isupov, A. Chung, N. Coffey, and L. Avruch, “Practical applications of balanced steady-state free-precession (bssfp) imaging in the abdomen and pelvis,” *Journal of Magnetic Resonance Imaging*, vol. 45, no. 1, pp. 11–20, 2017.
- [50] K. Scheffler and S. Lehnhardt, “Principles and applications of balanced ssfp techniques,” *European radiology*, vol. 13, no. 11, pp. 2409–2418, 2003.
- [51] D. D. Traficante, “Relaxation. can t2, be longer than t1?” *Concepts in Magnetic Resonance*, vol. 3, no. 3, pp. 171–177, 1991.
- [52] M. Katoh, A. Buecker, M. Stuber, R. W. Günther, and E. Spuentrup, “Free-breathing renal mr angiography with steady-state free-precession (ssfp) and slab-selective spin inversion: initial results,” *Kidney international*, vol. 66, no. 3, pp. 1272–1278, 2004.
- [53] M. F. Brasz, “Renal artery segmentation methods for wilms tumors review of methods, experimental phase and recommendation,” 2018, unpublished.
- [54] A. F. Frangi, W. J. Niessen, K. L. Vincken, and M. A. Viergever, “Multiscale vessel enhancement filtering,” in *International conference on medical image computing and computer-assisted intervention*. Springer, 1998, pp. 130–137.
- [55] T. Jerman, F. Pernuš, B. Likar, and Ž. Špiclin, “Beyond frangi: an improved multiscale vesselness filter,” in *Medical Imaging 2015: Image Processing*, vol. 9413. International Society for Optics and Photonics, 2015, p. 94132A.

- [56] J. C. Bezdek, R. Ehrlich, and W. Full, "Fcm: The fuzzy c-means clustering algorithm," *Computers & Geosciences*, vol. 10, no. 2-3, pp. 191–203, 1984.
- [57] R. Adams and L. Bischof, "Seeded region growing," *IEEE Transactions on pattern analysis and machine intelligence*, vol. 16, no. 6, pp. 641–647, 1994.
- [58] M. Kass, A. Witkin, and D. Terzopoulos, "Snakes: Active contour models," *International journal of computer vision*, vol. 1, no. 4, pp. 321–331, 1988.
- [59] T. F. Chan and L. A. Vese, "Active contours without edges," *IEEE Transactions on image processing*, vol. 10, no. 2, pp. 266–277, 2001.
- [60] J. Canny, "A computational approach to edge detection," in *Readings in computer vision*. Elsevier, 1987, pp. 184–203.
- [61] S. D. Popov, N. J. Sebire, and G. M. Vujanic, "Wilms' tumour–histology and differential diagnosis." Codon Publications, 2016.
- [62] M. Buser, "Semi-automatic 3d wilms tumour segmentation, development of diffusion weighted aided t2 watershed segmentation," 2019, unpublished.
- [63] S. Müller, I. Farag, J. Weickert, Y. Braun, J. Dobberstein, A. Lollert, H. Andreas, and N. Graf, "Benchmarking wilms tumor in multi-sequence mri data: Why does current clinical practice fail? which popular segmentation algorithms perform well?" *unpublished*, 2019.
- [64] A. J. Murphy and A. M. Davidoff, "Bilateral wilms tumor: A surgical perspective," *Children*, vol. 5, no. 10, 2018. [Online]. Available: <https://www.mdpi.com/2227-9067/5/10/134>
- [65] A. M. Davidoff, R. B. Interiano, L. Wynn, N. D. Santos, J. S. Dome, D. M. Green, R. C. Brennan, M. B. McCarville, M. J. Krasin, K. Kieran *et al.*, "Overall survival and renal function of patients with synchronous bilateral wilms tumor undergoing surgery at a single institution," *Annals of surgery*, vol. 262, no. 4, p. 570, 2015.
- [66] I. S., E. Hervieux, H. Boutroux, F. Becmeur, H. Ducou le Pointe, G. Leverger, and G. Audry, "Preoperative 3d reconstruction images for paediatric tumours: Reliability, advantages and drawbacks," in *SIOP*, 2019, abstract, unpublished.
- [67] L. Adams, B. Ralla, G. Engel, G. Diederichs, B. Hamm, J. Busch, F. Fuller, and M. Makowski, "Assessing venous thrombus in renal cell carcinoma: preliminary results for unenhanced 3d-ssfp mri," *Clinical radiology*, vol. 73, no. 8, pp. 757–e9, 2018.
- [68] S. McMahan and R. Carachi, "Wilms tumor with intravascular extension: A

- review article,” *Journal of Indian Association of Pediatric Surgeons*, vol. 19, no. 4, p. 195, 2014.
- [69] A. M. Davidoff, D. W. Giel, D. P. Jones, J. J. Jenkins, M. J. Krasin, F. A. Hoffer, M. A. Williams, and J. S. Dome, “The feasibility and outcome of nephron-sparing surgery for children with bilateral wilms tumor: The st. jude children’s research hospital experience: 1999–2006,” *Cancer*, vol. 112, no. 9, pp. 2060–2070, 2008.
- [70] J. H. Aldrink, N. G. Cost, D. J. McLeod, D. G. Bates, J. R. Stanek, E. A. Smith, and P. F. Ehrlich, “Technical considerations for nephron-sparing surgery in children: what is needed to preserve renal units?” *Journal of Surgical Research*, vol. 232, pp. 614–620, 2018.
- [71] S. Emad-Eldin, O. Abdelaziz, and T. A. El-Diasty, “Diagnostic value of combined static-excretory mr urography in children with hydronephrosis,” *Journal of advanced research*, vol. 6, no. 2, pp. 145–153, 2015.
- [72] A. Wefer, J. Wefer, B. Frericks, M. Truss, and M. Galanski, “Advances in uroradiological imaging.” *BJU international*, vol. 89, no. 5, pp. 477–87, 2002.
- [73] C. E. Morin, M. P. McBee, A. T. Trout, P. P. Reddy, and J. R. Dillman, “Use of mr urography in pediatric patients,” *Current urology reports*, vol. 19, no. 11, p. 93, 2018.
- [74] T. Ohno, H. Isoda, A. Furuta, and K. Togashi, “Non-contrast-enhanced mr portography and hepatic venography with time-spatial labeling inversion pulses: comparison at 1.5 tesla and 3 tesla,” *Acta radiologica open*, vol. 4, no. 5, p. 2058460115584110, 2015.
- [75] R. A. Nievelstein, I. M. van Dam, and A. J. van der Molen, “Multidetector ct in children: current concepts and dose reduction strategies,” *Pediatric radiology*, vol. 40, no. 8, pp. 1324–1344, 2010.
- [76] A. S. Lundervold and A. Lundervold, “An overview of deep learning in medical imaging focusing on mri,” *Zeitschrift für Medizinische Physik*, vol. 29, no. 2, pp. 102–127, 2019.
- [77] A. Yaman, “Gettransformmatrix,” <https://www.mathworks.com/matlabcentral/fileexchange/24277-gettransformmatrix>, MATLAB Central File Exchange, May 2019.

# Glossary

- TI** Inversion Time. viii, 12, 13, 15, 18, 19, 43, 49,
- FOV** Field of View. ix, 6, 14–19, 21, 26, 28, 36, 45,
- WT** Wilms Tumour. 1–3, 6–8,
- uWT** unilateral WT. 1–3, 6, 28,
- bWT** bilateral WT. 1–3, 6, 7,
- OS** Overall Survival. 1–3,
- SIOP-RTSG** Renal Tumour Study Group of the International Society of Paediatric Oncology. 1, 3,
- RN** Radical Nephrectomy. 2, 3,
- NSS** Nephron Sparing Surgery. 2–7, 45–48,
- ESRD** End-Stage Renal Disease. 2,
- EFS** Event-Free Survival. 2,
- COG** Children’s Oncology Group. 3,
- MRI** Magnetic Resonance Imaging. 4, 8, 15, 19, 25, 28, 33, 44, 50, 51, 53, 62,
- SIOP** International Society for Paediatric Oncology. 4,
- CTA** Computed Tomography Angiography. 4, 34, 41, 46,
- MRA** Magnetic Resonance Angiography. 4, 5, 25, 26, 36, 41, 45–47, 50,
- T** Tesla. 4, 15, 25, 28,
- CE-MRA** Contrast-Enhanced MRA. 4, 5, 8, 25–30, 41–43,
- GBCM** Gadolinium-Based Contrast Medium. 5, 22, 42, 43, 46,
- NC-MRA** Non Contrast-Enhanced MRA. 5–9, 26, 30, 34, 36, 37, 41, 43, 45, 46, 49,
- b-SSFP** Balanced Steady-State Free Precession. 5, 6, 11, 12, 19–21, 25–30, 33–36, 41–43, 46, 49, 50, 53,

**UCS** Urine Collection System. 7, 19, 21, 22, 33, 35, 45, 47, 49, 51,

**FA** Flip Angle. 11–16, 19,

**MIP** Maximum Intensity Projection. 15, 26–28,

**DICOM** Digital Imaging and Communications in Medicine. 19,

**ROI** Region of Interest. 19, 22, 26, 37,

**STL** Stereolithography. 19,

**VOI** Volume of Interest. 20–22, 35, 36,

**CNR** Contrast-to-noise ratio. 26–29, 41–43,

**SR** Segmentation Result. 34,

**GT** Ground Truth. 34,

**MRV** Magnetic Resonance Venography. 46, 49, 50,

**MRU** Magnetic Resonance Urography. 47, 49,

**MRP** Magnetic Resonance Portography. 50,